Spring 1-1-2018

Towards Fast Dual Frequency Comb Spectroscopy in Dynamic High Pressure Systems

Anthony Diego Draper
University of Colorado at Boulder, wanderer.anthony@gmail.com

Towards Fast Dual Frequency Comb Spectroscopy
in Dynamic High Pressure Systems
by
Anthony Diego Draper

A thesis submitted to the
Faculty of the Graduate School of the
University of Colorado in partial fulfillment
of the requirement for the degree of
Master of Science
Ann and H.J. Smead Department of Aerospace Engineering Sciences
2018

This thesis entitled:
Towards Fast Dual Frequency Comb Spectroscopy in Dynamic High Pressure Systems
written by Anthony Diego Draper
has been approved for the Ann and H.J. Smead Department of Aerospace Engineering Sciences

Assistant Professor Gregory Rieker

Professor Brian Argrow

Professor John Daily

Date_____

The final copy of this thesis has been examined by the signatories, and we find that both the content and the form meet acceptable presentation standards of scholarly work in the above mentioned discipline.

Draper, Anthony Diego (M.S., Aerospace Engineering)

Towards Fast Dual Frequency Comb Spectroscopy in Dynamic High Pressure Systems

Thesis directed by Assistant Professor Gregory B. Rieker

Laser absorption spectroscopy is a non-intrusive diagnostic tool particularly well-suited to investigate the dynamic and harsh conditions commonly found within combustion systems. By measuring the amount of light absorbed at specific wavelengths that are resonant with rotational-vibrational transitions in molecules, absorption spectroscopy gives a measure of the molecular population in particular quantum states. Experimental spectra are fit with a simulation generated from spectral line shape models combined with a spectroscopic database to infer species concentrations, temperature, and pressure. Dual frequency comb spectroscopy (DCS) with mode-locked frequency comb lasers is an emerging form of absorption spectroscopy that yields both high resolution (<1 GHz) and broad bandwidth spectra (>10 THz) on rapid timescales (< 2 ms). There are two key challenges facing DCS in dynamic combustion environments. First, obtaining high signal-to-noise-ratio (SNR) spectra has traditionally involved coherently averaging hundreds of individual spectra over seconds to minutes before fitting. Second, at the high temperatures and pressures commonly found within combustion systems, the existing line shape models and spectroscopic databases are known to not capture all of the key molecular physics, thereby requiring empirical extension and validation. This work presents techniques to enable rapid DCS measurements of thermodynamic properties in dynamic high-pressure, high-temperature, environments through power optimization and apodization to improve the short-term SNR. A rapid compression machine at Colorado State University is instrumented with a portable DCS spectrometer and temperature is recovered at 704 μs resolution from 1-21 bar and 294-566 K. This demonstrates the ability of DCS to be applied to combustion-relevant timescales for both broad bandwidth and high resolution non-intrusive measurements of harsh systems. The design development of an optical testbed that creates a well-known, high-temperature, and high-

pressure environment is additionally discussed. This subsequently will enable determination of the accuracy limitations of existing molecular absorption models, as well as allow for model expansion. Together these abilities enable laser measurements to better evaluate and optimize combustion systems, including improved understanding of the underlying molecular processes. Proper understanding of the molecular dynamics will allow for instrumentation and quantification of more extreme environments such as inside rocket engines or the atmospheres of distant planets.

Dedication

This work is dedicated to the women in my life. My mom and grandmother for always believing in me and providing an environment of learning, exploration, and challenge. My girlfriend Julie for the continual enormous amounts of support and advice. And my middle school science teacher, Ms. Coveyduck, for inspiring my scientific curiosities.

Acknowledgements

I would like to thank Dr. Rieker for the incredible opportunity to perform research for him, and the invaluable guidance he has provided. I would also like to thank the Precision Laser Diagnostics Laboratory for the continuous support, numerous moments of laughter, and the ever-present possibility to teach me something new. Special thanks to Ryan Cole, Dr. Nazanin Hoghooghi, and Dr. Paul Schroeder for their sage advice and support.

CONTENTS

List of Tables

List of Figures

1. INTRODUCTION

1.1. Motivation

Infrared laser absorption spectroscopy is a useful technique for quantitative, nonintrusive measurement of gas temperature and species concentration in combustion systems [1]. Absorption spectroscopy measures the amount of light absorbed at specific wavelengths that correspond to rotational-vibrational transitions of the molecules in a gas mixture in order to determine the molecular populations in various quantum states. These populations can be linked back to temperature and species concentrations. The dynamic and harsh conditions found in many high-speed combustion systems place demanding requirements on laser absorption sensors. Specifically, the sensor must be able to quantify the absorption at high sensitivity and on short timescales. The ideal sensor would achieve these goals while also measuring over a broad frequency range at high resolution. Broad spectral bandwidth enables the measurement of multiple species that absorb at different frequencies, increases the temperature sensitivity and range by probing many rotational-vibrational energy levels, and allows the sensor to resolve absorption features over a large range of pressures and through spectral overlap of neighboring absorption transitions. This last capability is crucial as small molecules will exhibit narrow absorption features at ambient conditions which broaden and blend as the pressure increases.

The thermodynamic measurements are determined through fitting the experimental data, termed spectra, with simulations generated from spectral line shape models combined with a spectroscopic database. However, experimental data has shown that existing models and databases do not replicate absorption features exactly at higher temperatures and pressures [1,2]. In order to better understand and diagnose high pressure combustion systems, it is fundamental

to have models and databases that fully replicate the molecular dynamics. That is to say, while spectral simulations are lacking the unknown uncertainty of measurements increases. This understanding, and necessity for improvement, not only applies to combustion systems, but also has applicability with exoplanet research [3,4].

1.2. Research Contribution

Through this thesis, methods to enable fast DCS measurements of high pressure dynamic systems are developed and validated. Optical power is optimized to remain within the fast photodetector linarity limit yielding the highest short-term SNR without signal degredation. A simple post-processing application of an apodization technique is presented which then increases the short-term SNR even further. These improvements allow spectra, which were previously too noisy, to be analyzed for thermodynamic properties at short timescales. To fully expand the capabilities of DCS towards combustion systems, an optical testbed is also developed that allows for high quality absorption spectra to be obtained at elevated temperatures and pressures. The spectroscopic cell is designed with a pathlength of 45 cm, and has the ability to quantify nonlinear effects of the instrumentation. Absorption spectra of CO_2 are collected at a maximum pressure of 35 atm at 500 K, and at a maximum temperature of 750 K at 20 atm. These collected spectra represent the beginning of an expansive spectral parameter exploration.

1.3. Thesis Structure

This thesis will first discuss methodologies for obtaining fast DCS measurements of a dynamic high pressure environment. These methodologies are demonstrated through instrumenting a rapid compression machine (RCM) at Colorado State University (CSU) containing a CH_4-N_2 gas mixture, and unique treatment of the experimental spectra in post-processing. An apodization technique is evaluated and its implications to improve the short-term SNR are discussed. This reduces the spectral resolution of the dual-comb spectrometer, however the degree of apodization is selected to be able to resolve absorption features of the gas mixture across the entire compression process. Selectively choosing the degree of apodization then allowed for temperature of the mixture is recovered every 704 μs across a compression from 1-21 bar and 294-566 K. However, to fully realize fast DCS in dynamic high pressure systems, the existing spectral models and databases must be expanded.

The initial development of an optical testbed for developing absorption models at extreme pressure and temperature conditions is subsequently discussed. An engineering evolution of the subcomponent designs are presented, along with failure analysis and outcomes if applicable. These subcomponents are concluded with the system overview. System data is analyzed in an attempt to characterize the system capabilities. Correlations between the temperature pressure influences on system performance are also analyzed. Due to the high resolution and broadband nature of the dual-comb spectrometer, accurate absorption spectra are obtained. Lastly, a progression of CO_2 spectra is displayed demonstrating the ability of the sytem to experimentally improve existing spectral models and databases.

2. BACKGROUND

2.1. Laser Absorption Spectroscopy

Spectroscopy involves the study of how light interacts with matter, and absorption spectroscopy specifically studies how light is absorbed by matter. Due to the quantum mechanical nature of atoms and molecules, only discrete states of existence are possible. Furthmore, only discrete energy transitions between states may occur. These energy transitions correspond to either absorption or emission of radiation. Planck formulated the frequency dependence of these transitions as Eq. (2.1) where ΔE is the transition energy, h is Planck's constant, and ν is the frequency of light. This can additionally be expressed in terms of the speed of light, c, and the its wavelength λ.

$$\Delta E = h\nu = \frac{hc}{\lambda} \qquad (2.1)$$

The energy transitions for specific frequencies, termed lines, are furthermore split into three categories: rotational, vibrational, and electronic. Pure rotational transitions occur within the microwave region, vibrational and rotational-vibrational (ro-vibrational) transitions occur within the infrared (IR), and electronic and rovibronic within the visible and ultraviolet (UV) portions of the electromagnetic spectrum. This work focuses on near-IR ro-vibrational absorption spectroscopy, and an example simulated spectra is shown in Figure 1 (a). The uncertainty principle also dictates that the lines are not a perfect line, but instead replicates a Lorenztian profile as shown in Figure 1 (b).

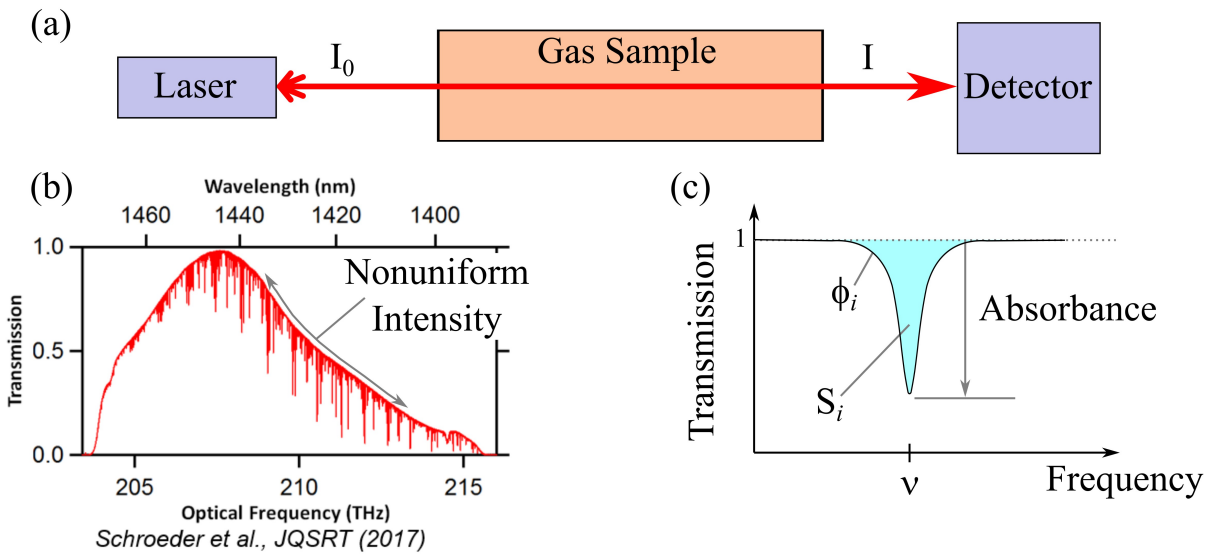

Fig. 1. Representative direct absorption spectroscopy diagram. (a) Laer beam interacting with gas sample of interest with unattentuated intensity I_0, and the detector receiving light intesntiy I. (b) Example transmission spectra. Nonuniform intensity profile is the non-uniform top structure of spectra. Thin downward lines are absorption lines. (c) Representative absorption feature.

Each of these profiles are referred to as absorption features, and can be determined by measuring the absorbance at different frequencies. The absorbance is found through the Beer-Lambert Law shown in Eq. (2.2) where I is the transmitted light intensity, I_0 is the light intensity before interacting with the sample, $S_i(T)$ is the line strength of transition i, $\Phi_i(T,P,\nu)$ is the line shape function of transition i, P is the pressure, χ_j is the mole fraction of species j, and L is the pathlength [5–7].

$$\text{Absorbance} = \ln\left(\frac{I}{I_0}\right) = -\sum_i S_i(T)\cdot\phi_i(T,P,\nu)\cdot\chi_j\cdot P\cdot L \qquad (2.2)$$

With a single diode laser, in general, the frequency is rapidly swept across the feature by varying the current or voltage. A photodetector on the other side of the sample then records the light intensity for the given frequency. Models and spectral databases contain the necessary

analytical forms and parameters to then replicate absorption profiles for a wide range of gases and combinations. Properties of the system can then be extracted by fitting a simulated spectra. The simulated spectra is generated, in part, through proper models and databases that define S_ν and Φ_ν. The line shape function and strength are also dependent on temperature and pressure, and will vary in different manners. However, it has been observed that the existing models and databases do not properly replicate the observed absorption features at elevated temperatures and pressures [2,8–10]. This results in unknown uncertainty when the thermodynamic properties are recovered.

2.2. Dual Frequency Comb Spectroscopy

Frequency combs are laser sources that emit many discrete, evenly spaced frequencies of light, often referred to as comb teeth. DCS is an emerging technique that uses two frequency combs and is capable of simultaneous broad bandwidth and high resolution [11]. In DCS, a frequency comb is interfered with a second comb having slightly different tooth spacing in a massively parallel optical heterodyne approach. This allows absorption to be resolved tooth-by-tooth, and for the data to be collected in the RF-domain with a single photodetector and no moving parts.

There are several classes of frequency comb that are currently capable of robust, portable operation: fiber mode-locked, modulator, and quantum cascade laser (QCL) combs. Mode-locked combs exhibit a train of short pulses comprising many thousands of comb teeth with optical frequency spacing matching the pulse repetition rate of the laser [12]. The intensity of the pulses lend themselves to nonlinear processes, and thus mode-locked combs are capable of

nonlinear broadening to thousands of wavenumbers. Typically, the comb tooth spacing is very fine (0.003-0.03 cm^{-1}), as larger spacing requires high pulse repetition rate, which in turn would lead to short laser cavities and reduced peak power for nonlinear broadening.

Modulator combs are generated by electro-optic modulation of continuous-wave lasers [13,14]. The tooth spacing is given by the frequency of the RF source driving the modulators, thus the spacing can be tuned from 10^{-4} cm^{-1} to 1 cm^{-1}. However, the bandwidth of these combs is typically limited to a few wavenumbers and requires more complex approaches to achieve a broad bandwidth [15]. QCL frequency combs are semiconductor sources emitting in the mid-IR and THz. They have modest bandwidth (40-100 cm^{-1}) in the mid-IR (1111-1667 cm^{-1}), with comparably large mode spacing (0.25-0.5 cm^{-1}), which leads to a relatively small number of comb teeth across the spectrum (a few hundred).

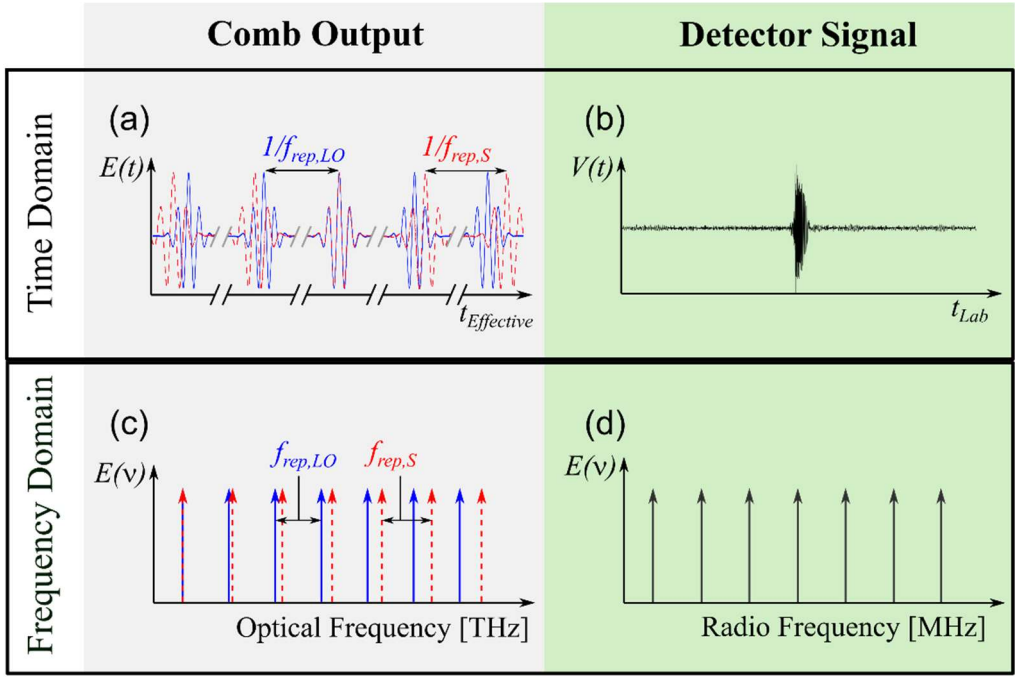

Fig. 2. Diagram showing the time and frequency domain representation of dual frequency comb spectroscopy. (a) Effective time domain schematic of femtosecond comb pulses originating from

combs with different repetition rates, where the pulses of one comb "step through" the pulses of the other comb. The signal comb is shown in dashed red and the local oscillator comb in blue. (b) The time domain signal as recorded by the photodetector is a cross-correlation of the comb pulses – an interferogram – formed in laboratory time and with a "centerburst" when the pulses of the two combs are overlapping. (c) The comb teeth of the two combs represented in the optical frequency domain. The two comb repetition rates are fixed such that a unique heterodyne beat in the RF-domain is formed from pairs of comb teeth. (d) Individual comb teeth are resolved in the RF-domain by taking the Fourier Transform of the interferogram shown in (b).

A representative diagram of mode-locked DCS is shown in Figure 1. DCS with mode-locked lasers is most easily described in the frequency domain, where each comb spectrum consists of evenly spaced frequency modes (teeth). Two frequency combs are phase locked to a stable reference such that the signal comb has repetition rate $f_{rep,S}$ and the second, local oscillator, comb has repetition rate $f_{rep,LO}$, where $f_{rep,S} - f_{rep,LO} = \Delta f_{rep}$. Moving across the spectrum, the optical frequency of each pair of fast and slow comb teeth differ by a frequency $n\Delta f_{rep}$, where n is an integer number of tooth pairs from the point where the frequencies of a pair of teeth exactly overlap. This difference frequency is detected on a photodiode as a heterodyne beat frequency, effectively mapping the magnitude of each pair of comb teeth from the optical domain into the RF-domain as shown in Figure 2 (d).

DCS can be described equivalently in the time domain as two femtosecond pulse trains with different repetition rates. In the frame of a pulse emitted by the signal comb, pulses from the local oscillator comb iteratively step through the signal comb pulse at an effective time step of $\Delta T_E = \Delta f_{rep}/(f_{rep,S} f_{rep,LO})$ [16]. These pulse trains are incident on a photodetector, such that they form a cross-correlation between the electric fields of the different comb pulses (termed an interferogram), that can be seen in Figure 2 (b), which exhibits an intense centerburst when the pulses of the combs are overlapping in time. The interferogram is digitized by commercial electronics with a laboratory time step between data points of $\Delta T_L = 1/f_{rep,LO}$. Each

interferogram is constructed of $N = f_{rep,LO}/\Delta f_{rep}$ individual points, and thus the laboratory time to acquire a single interferogram is given by $t_{acq} = 1/\Delta f_{rep}$. The frequency domain spectrum described in the preceding paragraph is the Fourier transform of the time domain interferogram. A nonuniform intensity profile develops from the nonlinear optical processes within the spectrometer. To account for this variation, a non-absorbing baseline is fitted that corrects the measure absorbance. Typically this baseline is removed utilizing a low-order polynomial fitting routine described in [2] and the supplement to [17]. The incident dual-comb spectrum can also be measured as a means of accounting for the non-absorbing baseline. A more detailed description of the DCS method applied here is given in [11,16,18].

2.3. Rapid Compression Machines

RCMs are typically used for laboratory studies of fuels and combustion kinetics, as well as sensor validation in realistic, engine-like conditions [19]. RCMs generally utilize one or more pneumatically driven pistons that, when released, rapidly compress a gas sample with a compression ratio of 10 to 20, resulting in elevated compressed pressures and temperatures (e.g. 10 to 30 bar, 500 to 1000 K) The compression process can occur in as little as 2 ms, and thus is often considered analogous to a single compression stroke of an internal combustion engine [19]. The combination of short timescales with rapidly varying thermodynamic conditions provides a realistic and demanding system in which sensors can be tested and validated.

The temperature evolution during the compression process is of particular interest for chemical kinetics studies due to its relation to reaction rate constants [5]. The temperature during the compression event T, can be approximated by Eq. (2.3) from a known initial temperature T_0,

initial pressure P_0, the measured pressure during the compression $P(t)$, and the ratio of specific heats of the gas mixture γ [20].

$$\ln\left(\frac{P(t)}{P_0}\right) = \int_{T_0}^{T(t)} \frac{\gamma}{\gamma - 1} \frac{dT}{T} \qquad (2.3)$$

This equation relies on the so-called adiabatic core assumption, namely that the compression occurs on such a short timescale that there is negligible heat transfer from the gas. This assumption will lose validity due to aerodynamic mixing during the compression as well as due to any chemical reactions that may occur [3-4]. After a compression the pistons reach their final position, and the gas has additional time for heat transfer with the RCM walls, further deviating from the idealized process. Consequently, accurate temperature measurements are vital for combustion studies both in the time period of the compression process, as well as after the end of compression when the pistons are in their final position.

2.4. Laser Absorption Spectroscopy in Engine-Like Environments

Many laser absorption sensors with narrow wavelength coverage have been demonstrated in rapid compression and shock tube environments with high sensitivity and time resolution [5,22]. Narrowband sensors observe a few select absorption features of a single species that have favorable temperature dependence within a range of interest. As the spectral bandwidth is small, pressure broadening effects can cause the absorption feature linewidth to exceed the measurement range. Together, these features create bounds on the species coverage and usable temperature and pressure ranges of the laser sensor.

Recently, a number of studies have published broadband absorption spectrometers to measure temperature within harsh environments such as an RCM. Because broadband spectroscopy observes many absorption features, these techniques circumvent the limitations imposed by temperature sensitivity of particular features and pressure broadening that challenge narrowband sensors. The broadband nature additionally raises the possibility of multispecies monitoring. These sensors have relied upon external cavity diode lasers [23] or techniques such as Fourier domain mode locking [24] and supercontinuum generation [25,26] to record absorption spectra spanning hundreds of wavenumbers. Notably, Werblinski et al. demonstrate supercontinuum absorption spectroscopy in fired [25] and non-fired [26] RCMs. The authors record spectra spanning more than 500 cm^{-1} at a rate of 10 kHz to measure time histories of temperature, pressure, and water vapor mole fraction in the compressed gas through a first derivative fitting approach. So far, broadband approaches in rapidly varying environments have limited spectral resolution (e.g. ~0.8–2.0 cm^{-1} [23–26]) that can limit the published results to pressures above 6 bar, below which the spectrometer resolution matches or exceeds the linewidth of the absorption features.

2.5. Dual Frequency Comb Spectroscopy at Short Timescales

For a single dual-comb spectrum, the SNR in most cases is limited by the dynamic range of the detection system. In practice, the comb power striking the detector must be reduced to below the point where nonlinearities arise near detector saturation. Thus optimizing the power-per-comb-tooth striking the detector achieves the best noise characteristics. Comb systems operating with a small number of modes over a limited range, such as QCL and most modulator

combs, are therefore capable of high short-term SNR at the expense of resolution and/or bandwidth. Mode-locked combs with broad bandwidth and close tooth spacing place many more comb modes on the detector, spreading the power-per-mode and reducing short-term SNR, but with much higher bandwidth and resolution. At long timescales, the achievable SNR for DCS is driven by the ability to coherently average measured spectra. The ultimate SNR is therefore driven more by comb stability or the ability for software to correct for stability. Consequently, absorption spectra for mode-locked DCS are typically averaged on the order of seconds to minutes to reach very high SNR. These constraints have generally positioned femtosecond mode-locked comb sources for broadband multispecies measurements in applications with relaxed time resolution.

2.6. Spectral Parameter Estimation at High Temperatures and Pressures

Much of the existing work of absorption properties at high temperatures has been performed near room pressure. Similarly, many high pressure studies occur near room temperature. When combining the two extremes the pathlengths diminish as shown in Figure 3 [9,27,28,28–39]. For example, many of the cells capable of 40 atm or above, at temperatures greater than 400 K, have pathlengths within the range of 2-5 cm. Another existing measurement overlaps with the present design specifications presented here, however the pathlength is roughly six times shorter [30]. As noted in Eq. (2.2), the pathlength directly influences the absorbance. For a greater pathlength a higher SNR is achieved, which subsequently reduces the amount of time needed to acquire data. A decreased acquisition time has engineering benefits as well, as the

cell needs to experience the harsh environment for less amounts of time. However, the downside is that typically larger cells incur greater amounts of stress.

The larger pathlength cells in the bottom left of Figure 3 are mostly implemented with multipass cells to achieve greater light interaction with the sample. These greatly increase the pathlength by reflecting the beam path through the sample hundreds to thousands of times. However, there are disadvantages at high temperatures and pressures. Only certain gas samples may be analyzed, as the gas is generally in direct contact with the mirrors, and they may only operate to a certain temperature limit.

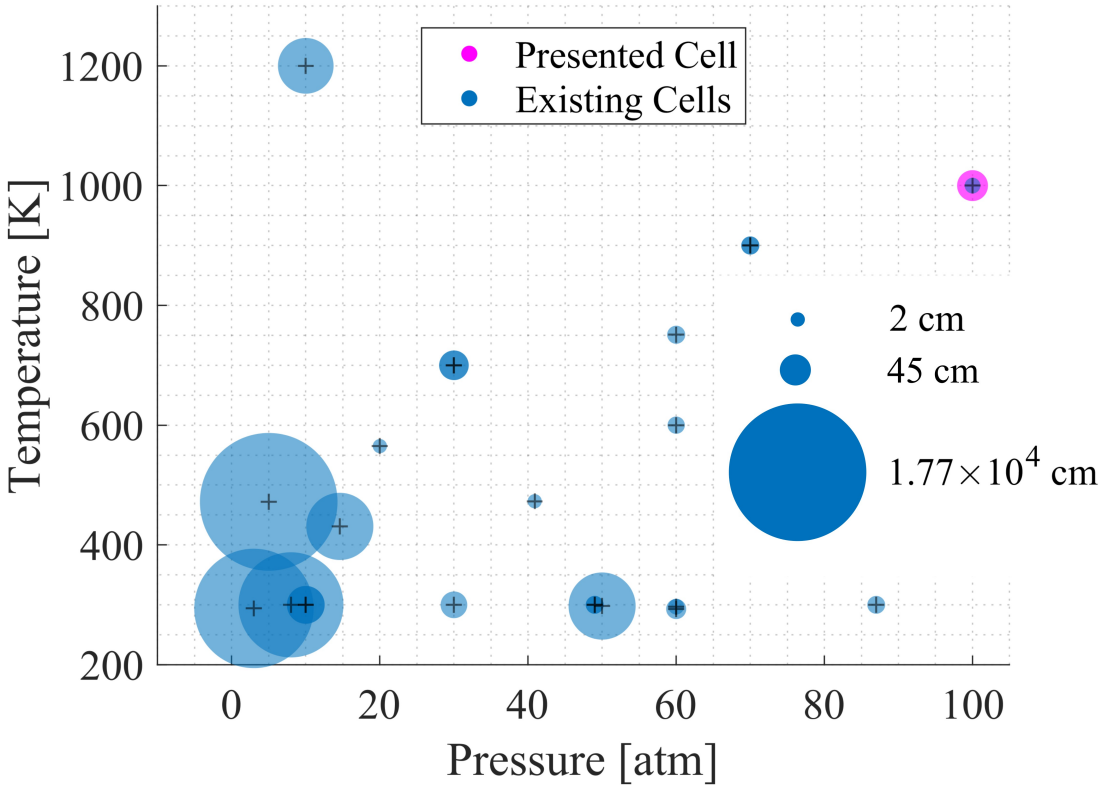

Fig. 3. Existing high-temperature, high-pressure, spectroscopic cell designs. Blue denotes existing cells, with the radius varying linearly with available pathlength [9,27,28,28–39]. Magenta is the design presented in this thesis with the marker radius also on the same pathlength scale.

3. MEASUREMENTS IN A RAPID COMPRESSION MACHINE

As mentioned above, the short term SNR of DCS is typically limited due to the low optical power-per-comb-mode. As such, previous practical deployments of mobile, mode-locked dual-comb spectrometers [1,40] typically average for 60-120 seconds to build high SNR. In order to resolve transient combustion phenomena, this averaging time must be decreased by upwards of a factor of 10,000. The first step to increasing the short-term SNR is to optimize the incident power on the photodetector. The approach is to maximize the power-per-comb-tooth (and thus the SNR) on the detector by filtering all comb teeth outside of the spectral region of interest, and to optimize the optical power incident on the photodetector such that it is operated just below the power level where detector non-linearity becomes large.

The short-term SNR for mode-locked DCS can be further increased by applying an apodization technique to the measured interferograms in post-processing. Most of the signal of interest in DCS is collected during the centerburst of the interferogram: when the pulses from the two combs are overlapping in time on the detector. The rest of the interferogram is still important to collect in order to obtain the right number of points for a full, comb-tooth-resolved spectrum, and because one must wait for the pulses of the two combs to overlap again. Apodization multiplies a function with the interferogram in order to retain the signal around the centerburst while filtering out the noise on the rest of the interferogram, which would subsequently become noise in the frequency domain. However, the cost of this technique is the addition of an instrumental line shape in the resulting absorption spectrum [7]. In this work, we apodize the interferograms with a boxcar function to increase the short-term SNR. The instrument line shape

resulting from a boxcar apodization function is described analytically as Eq. (3.1) where Δ_E is the HWHM of the boxcar function in effective time, and ν is the frequency.

$$f(\nu) = 2\Delta_E \mathrm{sinc}\left(2\pi\Delta_E \nu\right) \qquad (3.1)$$

Thus, the instrument line shape is perfectly known, and can therefore be applied to the absorption model that is used to fit the data. In order to demonstrate the feasibility of this method to a fitting routine with a spectral database, a 1 bar and 300 K CO line near 6297.5 cm^{-1} was measured in a static configuration with the fiber mode-locked dual-comb spectrometer discussed in the following section. A boxcar apodization was applied to both the experimental data and the HITRAN 2016-based absorption model. Figure 4 shows the agreement between the apodized model and measurement. As the instrument line shape is a known analytical function, the model replicates the effects of apodization exactly. Therefore, the outcome of a fitting routine used to determine the temperature or species concentration is unbiased by the addition of the instrument line shape.

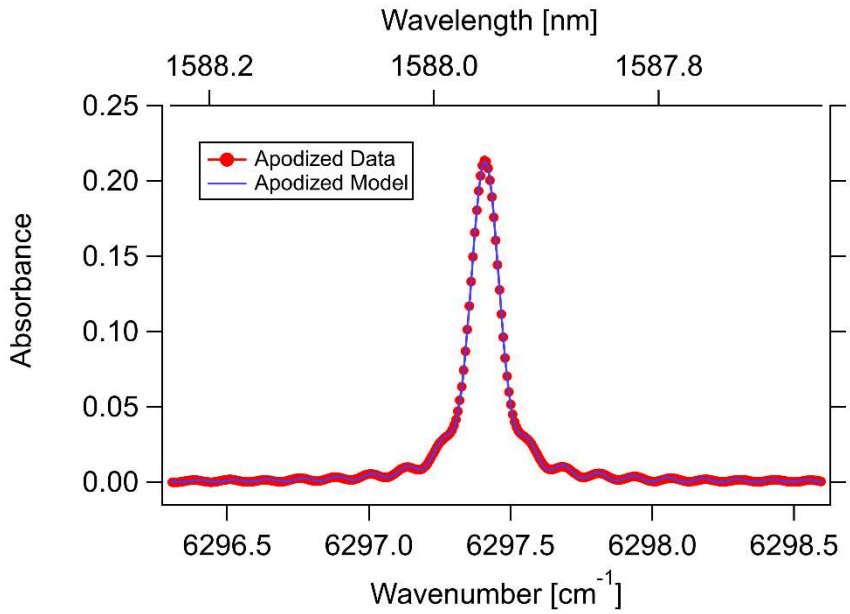

Fig. 4. Measured CO absorption feature near 6297.5 cm^{-1},with the same apodization applied to the measured interferogram (red) and the model (blue). The instrument lineshape from apodization is apparent, but is well captured by the model.

3.1. Experimental Setup

The RCM employed in this work was manufactured by Marine Technologies Ltd., and is housed in the Engines and Energy Conversion Laboratory at Colorado State University (CSU). The RCM employs dual piston design with creviced pistons that reduce the effects of aerodynamic mixing during the compression process [20,41], and was configured for a compression ratio of 12.5. Optical access to the combustion chamber is provided through two sapphire windows with a 3° wedge to discourage etalon interference effects. Gas pressure is measured before the compression process using an Omega DPG409 pressure transducer (accuracy 0.08% of reading), and monitored during the compression stroke using a Kistler 603B pressure sensor (accuracy 1% of reading). A detailed description of the CSU RCM facility can be found in [41,42].

A near-IR mobile dual-comb spectrometer [1,40,43] was phase locked with $\Delta f_{rep} = 2837\ Hz$, giving a single spectrum acquisition time of 352 μs. The laser light was filtered to cover 5967-6133 cm^{-1}, and an amplifier boosted the power in this frequency region up to the optimal range for the detector. The point spacing of the spectrum is set by the laser repetition rates to be 0.0068 cm^{-1}, which results in 24345 individually resolved comb teeth accessible for fitting. Light from the DCS was delivered with singlemode fiber to the RCM, collimated, and passed though the 4.63 cm combustion chamber. Laser light leaving the RCM is incident on a DC-coupled fast photodetector (ThorLabs PDA10CF), low-pass filtered (100 MHz bandwidth), and recorded with a 250 MS/s digitizer. A schematic of this experimental configuration is shown in Figure 5.

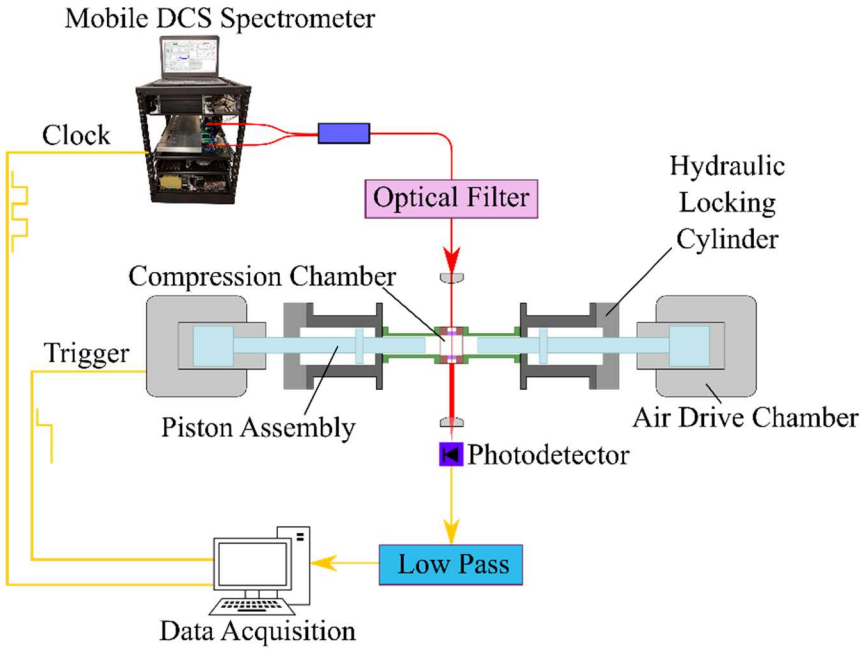

Fig. 5. Schematic of experimental setup. The mobile DCS supplies light via single-mode fiber to a collimator, which transmits the light through the RCM combustion chamber, and is then received through a convex focusing lens onto a fast photodetector. The resulting signal is low-pass filtered before being collected with the data acquisition system. The spectrometer also provides a clock signal to the data acquisition, and the RCM start switch is linked to enable synchronous collection.

The RCM combustion chamber was maintained at 294 ± 0.5 K, the pistons retracted and locked, and the chamber evacuated to 6.9 ± 0.8 mbar. A vacuum dataset was collected to aid in baseline correction in post-processing before compression. Subsequently, CH_4 was first added to the chamber, and then N_2, to give an initial pressure of 1001 mbar, with a CH_4 mole fraction of 0.750. Data collection was triggered synchronous to the RCM pistons being released via a common start signal. Time-domain interferograms were collected during the compression process through an automated LabVIEW program.

3.2. Results and Analysis

3.2.1. Data processing

Every two interferograms measured through the RCM were averaged for an overall measurement time resolution of 704 µs. A boxcar apodization HWHM of $\Delta_E = 229\ ps$ was applied to each binned interferogram, yielding a FWHM of the instrument line shape of 0.088 cm^{-1}. The spectral resolution with the instrument line shape can be estimated from Rayleigh's definition as $1/\Delta_E = 0.15\ cm^{-1}$ [7,16], which yields the experimental spectral resolution. This degree of apodization was selected in order to maintain the ability to resolve the CH_4 absorption features at 1 bar and 298 K before the RCM compression process.

Apodized interferograms were subsequently Fourier transformed to yield the CH_4 transmission spectrum through the RCM. Each transmission spectrum was baseline corrected using the vacuum background dataset and converted to absorbance units with Beer's law. A polynomial baseline fitting routine (described in [2] and the supplement to [17]) was used to correct residual baseline irregularities caused by subtle differences between the vacuum

background and compression datasets. Experimental spectra at the initial conditions are shown in Figure 6 to illustrate the effect of apodization. The resulting SNR benefit is dramatically evident. From the zoom view shown in Figure 6 (b), one can see the emergence of the CH_4 absorption feature from the noise using the apodization approach.

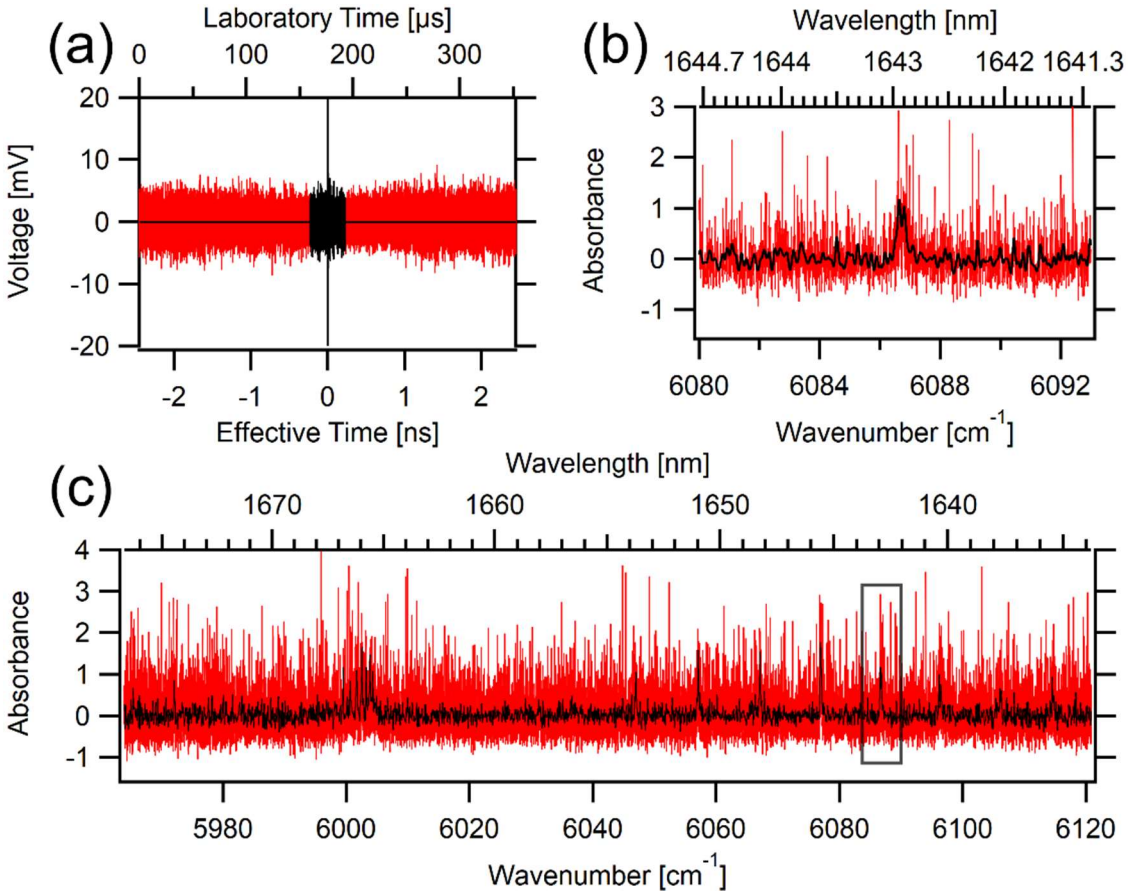

Fig. 6. Measured absorbance spectra at 1 bar and 294 K with 704 μs time resolution just prior to the compression. The red traces are the unapodized data and the black traces are apodized. (a) Interferogram with both the laboratory and effective timescales shown, (b) Zoomed CH_4 absorption feature for the region indicated on panel c, and (c) Full measured spectrum.

3.2.2. *Temperature Fitting*

A Levenberg-Marquadt algorithm was utilized to fit a model generated from the HITRAN 2016 database [44] with the Python HAPI package [45] to each baseline corrected spectrum. The mixture mole fraction and pressure were held constant and temperature was allowed to vary (with an initial guess from GASEQ calculations, described later). The resulting temperature fit is shown in Figure 7.

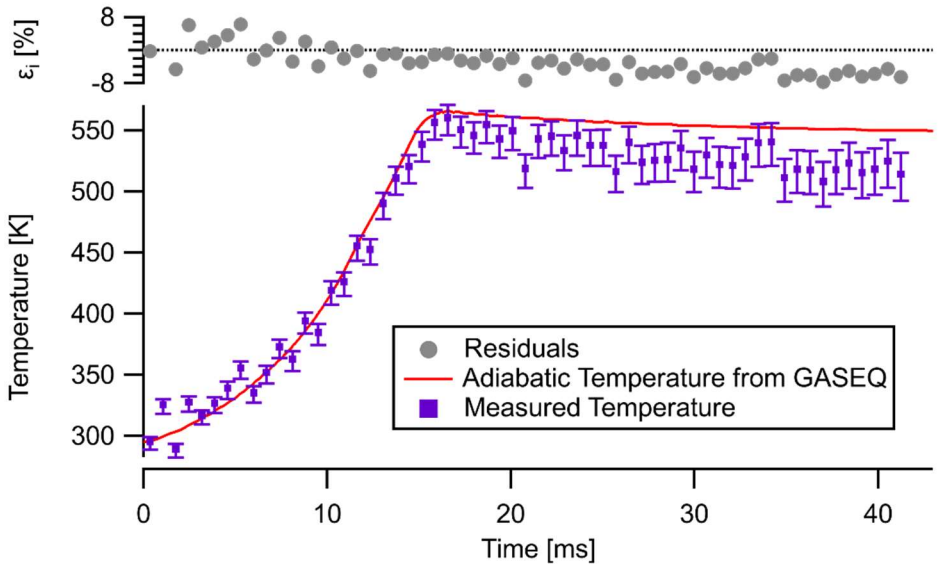

Fig. 7. DCS-measured temperature from broadband fitting of the apodized spectra (purple). The red trace is the adiabatic temperature calculated using GASEQ, while the gray represents the residual percent error.

Using the measured pressure, the compression temperature was calculated with GASEQ, a thermodynamic equilibrium software [46]. The measured temperature tracks well with the calculation during the compression process, 0 to 15 ms, and reaches a peak temperature 6 K lower than the 566 K predicted by GASEQ. This agreement is likely within the uncertainty of the GASEQ calculation, which we do not directly estimate here, but is affected by uncertainty in the initial temperature, gas composition, and measured pressure. The dual-comb measured

temperature decreases faster than the calculation once the pistons lock at the end of compression, ultimately reading approximately 19 K lower than the GASEQ predicted temperature after 25 ms. This deviation could arise from several effects. For example, heat loss and gas slippage from the compression chamber are not accounted for in GASEQ, though they do affect the result through the measured pressure. In addition, the formation of cold boundary layers can influence the path-averaged measured temperature to a value that is slightly different than the true average. With further detailed consideration of the results, it should be possible to determine the rate of heat loss. Having a measure of the rate of heat loss from the system also allows for system calibrations and compensations in subsequent RCM experiments.

The systematic uncertainty of the frequency comb measurement is represented by the uncertainty bars on Figure 7. The uncertainties of the pressure transducers, the physical tolerance stack-up of the path length, and the initial temperature were included as input values into the fitting routine to determine their influence on the measured temperature values. At the initial onset of the compression, the uncertainty is ±6 K, which increases to ±20 K at the end of data collection. The increase is a result of increasing pressure transducer uncertainty and the greater influence of the uncertainty in the initial conditions as one scales to higher compression.

The precision of the measurement was assessed using the residual between the measured and calculated values. The residual percent error was split into two sets: values leading up to and including the peak compression, and values from the peak until the end of the data set. The linear trends were removed from the residuals, the normality of the two sets verified through the Shapiro-Wilk test, and their standard deviations calculated. Up until the compression peak, the standard deviation of the residual percent error is ±3.1%, and ±1.5% afterwards. In the relatively

constant temperatures following the compression peak, the 1.5% residual percent error corresponds to approximately ±8.5 K measurement precision.

The high precision and low uncertainty is due in part to the broadband nature of the comb – the fit includes a very large number of comb teeth probing a large number of CH_4 absorption features, both of which lead to a robust fit. The dual-comb spectrometer is able to precisely resolve the CH_4 absorption features from atmospheric pressure all the way to the peak pressure of 21.15 bar.

3.3. Conclusion

We demonstrate high-speed, broadband, mode-locked dual frequency comb spectroscopy in an RCM by measuring the temperature of a CH_4-N_2 gas mixture with 704 μs time resolution. Absorption features were measured with 24345 comb teeth between 5197-6133 cm^{-1}. The short-term SNR of the portable spectrometer was improved through optical power optimization and the application of a boxcar apodization function to the interferograms in post-processing. The apodization technique introduced an exactly known instrument line shape, with a theoretical spectral resolution of 0.15 cm^{-1}. With this resolution, absorption features are fully resolved throughout the full range of temperatures and pressures encountered in the compression. The compressed gas temperature was measured using a broadband fitting algorithm with a model that incorporated the exact instrument line shape introduced from apodization. The fitted temperatures agree well with the predicted adiabatic values calculated from the measured pressure. This comparison shows a 6 K under prediction of the 566 K peak as well as indications of the breakdown of the adiabatic assumption after the end of compression. These results

indicate that mode-locked DCS can serve as a powerful diagnostic tool for broadband, high resolution spectroscopy in transient combustion environments.

The techniques presented in this thesis will see enhanced applicability when combined with rapidly evolving mid-IR mode-locked dual-comb technology. These spectrometers will leverage the bandwidth and fine mode spacing of existing DCS systems with higher sensitivity afforded by the stronger absorption cross sections characteristic of the mid-infrared. The increase in sensitivity will enable temperature measurements at higher time resolution, while the high bandwidth will enable multiple combustion-relevant species to be measured with a single spectrometer.

4. HIGH-TEMPERATURE, HIGH-PRESSURE, OPTICAL CELL

4.1. Introduction

The optical cell has undergone multiple design iterations over the three year project. A brief overview of the system in its entirety will be given here, along with the functional aspects of its operation. In the following section, a detailed engineering evolution of the subcomponents will be explained. Next, the optical layout of the assembled system is discussed. Then the system performance is evaluated from temperature, pressure, and detector voltage measurements from data collection campaigns. Lastly, experimental spectra collected with the optical testbed are presented and discussed, and conclusions are drawn.

Originally beginning as a Discovery Learning Apprenticeship project, the optical testbed was conceptualized by Dr. Paul Schroeder and Dr. Gregory Rieker to overcome spectroscopic model issues observed at elevated temperature and pressure. Measurements made within these harsh systems with near-IR DCS will then be rendered inaccurate until the models and databases are corrected. The prior RCM work was largely unphased by model degredation due to the relatively low temperatures and pressures exhibited. To enable future measurements at more extreme conditions, a system must be designed that has the ability to replicate high temperatures and high presusres in a highly repeatable manner. Additionally, as laser absorption spectroscopy measures a line-of-sight average, the spectroscopic cell must minimize temperature gradients that would otherwise skew the results. This partitions the design problem into two categories: temperature control and pressure control. The maximum capability of the system was specified to be 100 atm at 1000 K to ensure wide research potential, and is thusly referred to as the High-Temperature High-Pressure (HTHP) Cell.

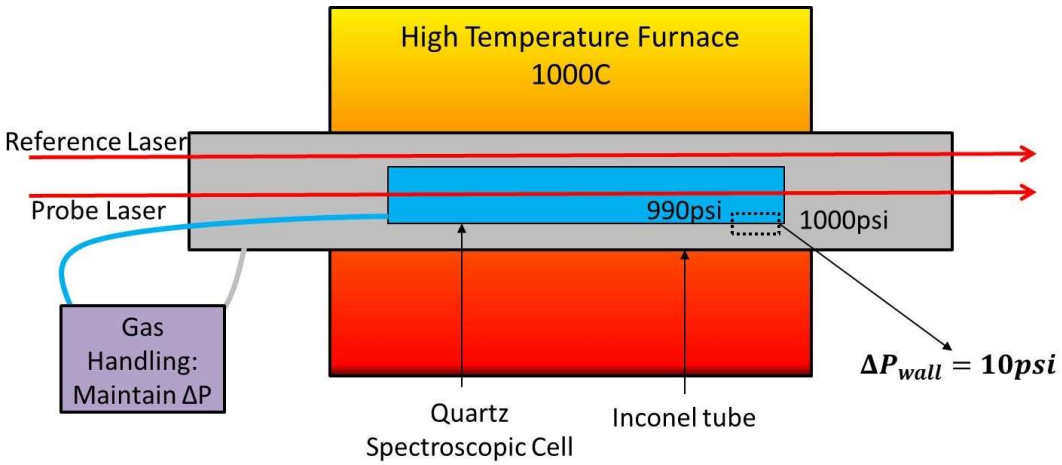

Fig. 8. Original high-temperature, and high-pressure, diagram given as part of Discovery Learning Apprenticeship proposal. The probe (experimental) laser beam is shown to intersect the quartz spectroscopic cell, while the reference laser passes through high temperature region without interacting with the sample. An Inconel tube is representative of what a high temperature pressure vessel may be composed of, but was not a design limitation. However, the high temperature furnace was already purchased for prior experiments and posed constraints on the possible design. The concept of keeping the quartz cell in compreison is represented by ΔP_{wall}.

A notable aspect of the original design that has persisted through system iterations is the cell-in-cell concept. Quartz was chosen to contain the process gas (i.e. the gas of interest) due to prior experience, as well as the ability to effectively tranmist the near-IR comb light. However, quartz is a brittle material and will fail in tension, but can survive reasonably well in compression. Therefore, a slight pressure differential is applied to the quartz cell to maintain compression while increasing the overall system pressure. This allows for the internal pressure to be maintained at 100 atm while the quartz only feels an order of magnitude less pressure differential provided by a bath gas. A drawback of this design is that the exterior pressure vessel must be able to retain high pressures, while also having to incur the high temperatures. This can be somewhat mitigated by moving the furnace to the interior of the pressure vessel so that the furnace insulation helps to shield the vessel wall. These concepts culminate in the current HTHP

Cell design consisting of a 45 cm quartz spectroscopic cell within the center of a SiC 17 kW furnace. The furnace is roughly 91 cm long, with a 23 cm diameter, and fits within the 183 cm long pressure vessel. An exploded view of the final system on a 4.27 m optical table is shown in Figure 9.

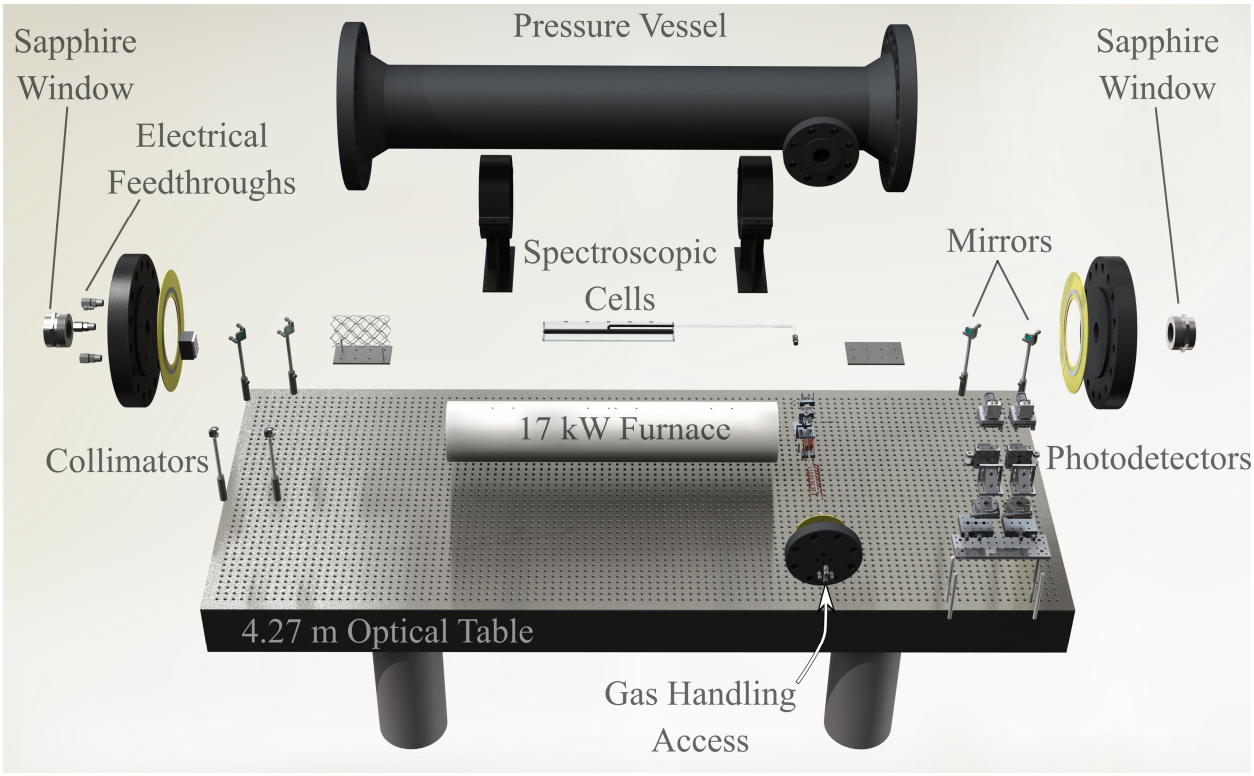

Fig. 9. Exploded view of high-temperature, high-pressure cell on 14 ft optical table. A three zone 6 kW resistance heater furnace is seen below two quartz spectroscopic cells, which are below the outer pressure vessel. Sapphire optical window fittings are shown on each farside of image. The collimators and mirror are shown on the left, while the photodetectors and additional mirrors on the right.

4.2. System Components and Design Evolution

4.2.1. Pressure Vessel

So-called supermetals such as Inconel or Haynes were originally studied as a means to satisfy the engineering constratins of the pressure vessel. These materials exhibit excellent high temperature performance, as indicative of their ubiquity within jet turbines, rocket engines, and power plants [47,48]. A factor in the performance that makes them suited for this application is the ability to resist mechanical creep and have long fatigue lifetimes. Mechanical creep is often observed within more ductile materials such as plastic where, for a given constant applied force, there is progressive strain that eventually deforms the material beyond the elastic limit.

Additionally, the fatigue life is of utmost importance as the system will be kept near its maximum design point for multiple hours, and will cycle between this and room temperature and pressure multiple times [49]. The fatigue rupture plot for Inconcel 740H, a candidate pressure vessel material, is shown in Figure 10.

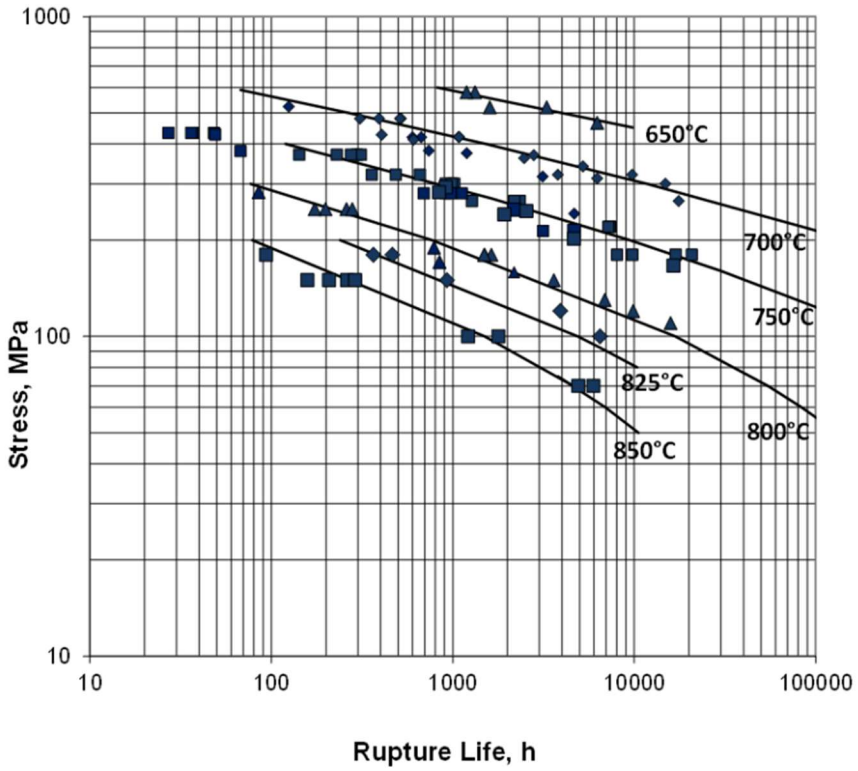

Fig. 10. Stress to produce rupture in Inconel 740H for given applied load lifetime. Increasing temperature dramatically reduces stress to produce yield given rupture life, however still exhibits high strength [50].

While Inconel, and other superalloys, offer the degree of strength required for a high temperature pressure vessel the system quickly grows in complexity and cost. To properly develop a pressure vessel that contains the required environment would require machining and welding a tenacious metal. Non-destructive testing would also need to be performed, such as x-ray analysis of the welds, for verification. Proper application of heat treatments to the alloys would also need to be implemented. All of this requiring an immense depth of knowledge. Due to the safety-critical nature of containing the high pressures, and design practicality, it was ultimately chosen to have an external company design, fabricate, and verify the pressure vessel. A diagram of the pressure vessel is shown in Figure 11.

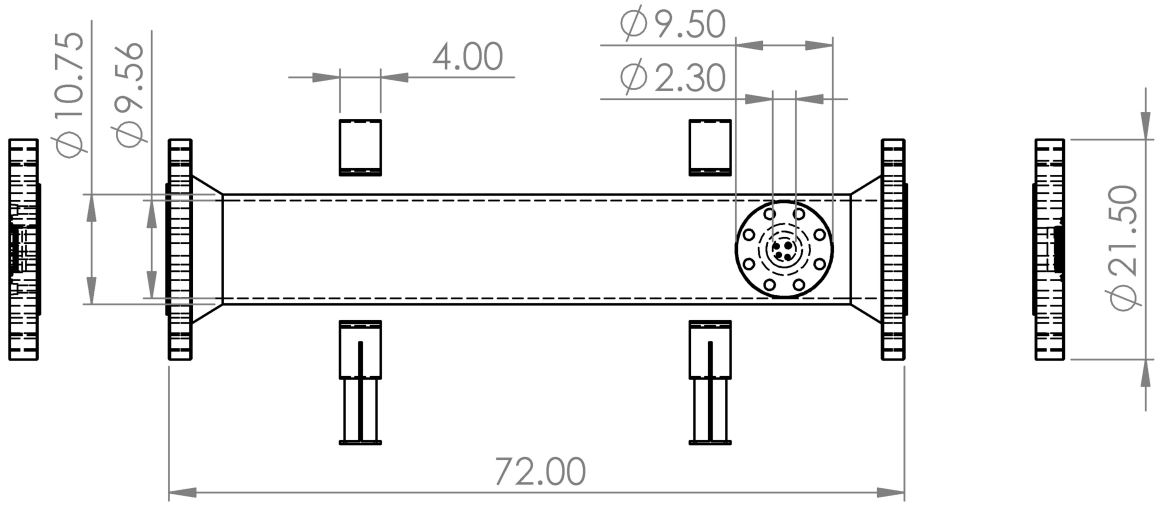

Fig. 11. Diagram of outer pressure vessel, with all dimensions in inches. The access port shown in bottom-right allows gas handling access to interior quartz cells. Left side of digram is referred to as power-side, while the right is gas-side.

Constructed out of steel, it was designed around a limitation of 300 °F on the interior surface to maintain structural integrity. Additionally, welding neck flanges were welded to the pressure vessel as they have the best fatigue and stress distribution characteristics. Large 21.5 inch OD flat-face flanges were secured to the welding neck flanges with 16 x 1.0 inch OD bolts, each torqued to 1356 N-m in a star pattern. A spiral wound gasket was utilized to maintain the outer flange seal and is known to exhibit resistance to leaks under cyclic loading. The gaskets also have a centering ring which helps to ensure proper gasket alignment, as well as prevent over-torquing. The entire pressure vessel, weighing 601 kg, is supported by two welded saddles which are bolted to a 4.27 m optical table with 16 total 1/4-20 bolts. Each flange weighing 115 kg is transported with an engine hoist and stored beneath the optical table when not in use. There is a small access port, again with a welding neck flange, protruding perpendicular to the

longitudinal axis of the pressure vessel. With an ID of 2.30 inches and a length of roughly 7 inches, this allows gas handling access inside the vessel.

4.2.2. Gas Handling

The primary objectives of the gas handling system are to properly maintain a pressure differential across the quartz spectroscopic cell, and to safely remove pressure if an emergency event occurs. To accomplish the first objective various design options were considered. Namely, the pressure can be controlled through two independent manual pressure regulators, two computer controlled pressure regulators, or a single manual pressure regulator can be used with a differential pressure regulator. The latter was chosen as it reduces the number of variables that need to be controlled, while also improving the system safety. The internal mechanism of a differential regulator is shown in Figure 12 [51].

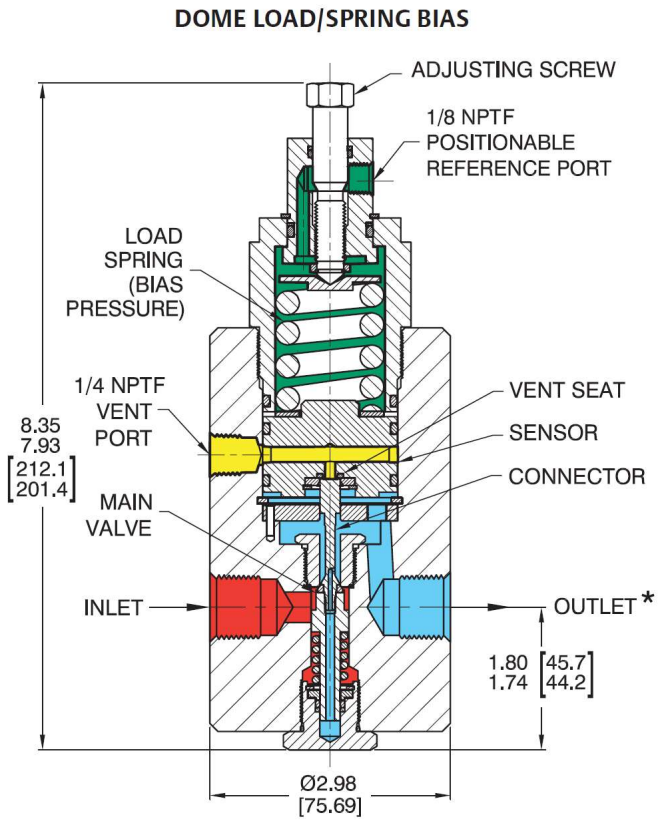

Fig. 12. Cross sectional diagram of differential pressure reducing regulator. Diagram borrowed from TESCOM™ 44-4000 datasheet [51].

A normal manual reducing pressure regulator operates on the condition that a handle controls the amount of spring force applied to a diaphragm or piston. The combination of downstream pressure, inlet pressure, and inlet bias spring oppose this set force and create a force balance between upstream and downstream pressures. Therefore, a decrease in the downstream pressure will open the diaphragm or piston to restore equilibrium. However, instead of a manually adjustable load spring, the differential regulator relies on a reference pressure in combination with a bias pressure spring. The differential pressure can then be adjusted manually with an adjusting screw so that a set differential pressure is maintained throughout operation. This allows for the process pressure to be sensed by the differential regulator, and then

proportionally open the bath gas to a predefined differential pressure and track the process pressure as it is increased. Ultimately this allows the operator to set the desired differential pressure, then only have to increase the process pressure while the bath gas tracks slightly higher. The particular differential regulator utilized, a Tescom 44-4000, also has self-contained venting so that when the process pressure reduces the bath gas vents while again maintaining the same differential. This concept was demonstrated with a roughly 1:12 subscale model by volume, with the pressure tracking performance shown below in Figure 13.

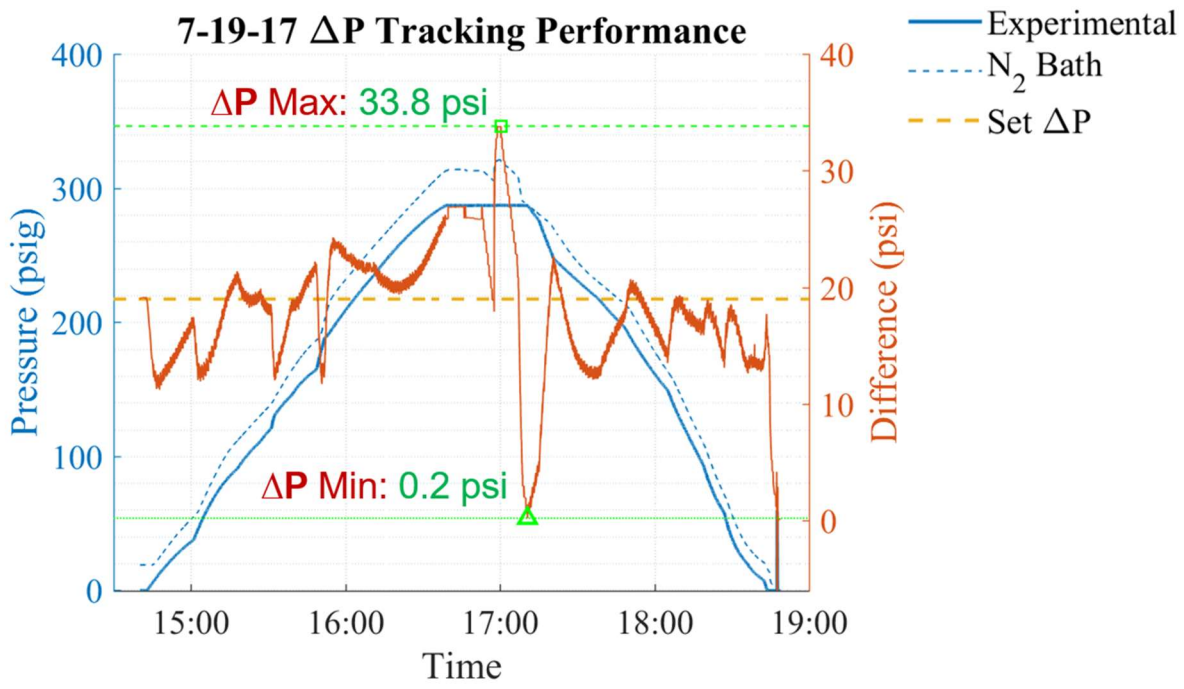

Fig. 13. Differential regulator tracking performance with subscale model on July 19th, 2017. A difference of 20 psi was set on the differential regulator and the experimental gas pressure increased. Venting tests were performed at approximately 17:00, and then the experimental pressure decreased.

It is likely that the small volume size, relative to the large industrial processes that the Tescom 44-4000 would normally encounter, created a higher sensitivity to changes in the dome loading pressure. Despite this, the tracking performance met the expectations for operation. The

large pressure change at roughly 17:00 corresponded to testing the sensitivity of the bias spring seating while changing from pressurization to depressurization. First, the N_2 bath gas was manually vented to verify and characterize that the differential regulator would refill the bath gas in response. Second, the process pressure was manually vented. It was discovered that while decreasing the process fluid, the differential will increase beyond the setpiont (i.e. the process pressure decreases while the bath gas remains the same) until the vent seal unseats and allows downstream venting.

Proportional relief valves (PRVs) are the other pivotal components of the gas handling design. The PRVs have a similar spring biasing mechanism, however they are meant to vent the upstream pressure if it exceeds a predefined setpoint. The exhaust port area is proportionally opened relative to how far the upstream pressure exceeds the setpoint and eventually fully opens to release all of the upstream gas. This allows the system to quickly dump the internal pressure before it exceeds the design limit of 100 atm. The overall process and instrumentation diagram (PID) is shown in Figure 14.

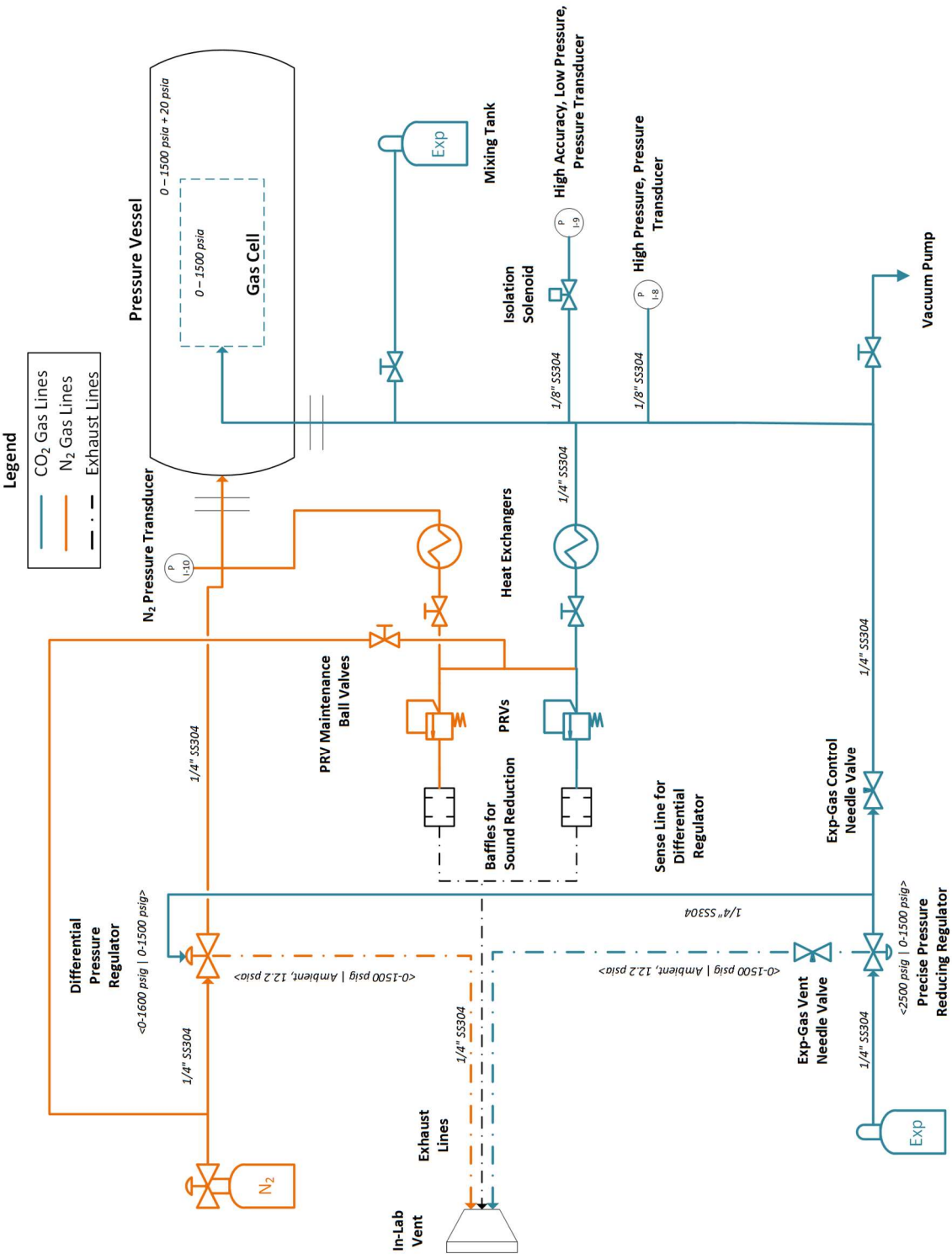

Fig. 14. Process and instrumentation diagram for gas handling system. The experimental tubing is shown in blue while the reference tubing is in orange. N_2 is shown as the reference gas, while in actuality this could be different.

Another key component is the needle valve on the experimental line downstream from the pressure regulator. This allows for the desired pressure to be set by the operator, then the needle valve slowly opened to adjust the gas flow to match the differential regulator through choking the flow. While this greatly enhances the controllability of the pressurization process, the ratio of the bath gas to the experimental volumes requires slow fill times. After multiple experiments, an average fill rate would result in roughly 240 psi/hr.

The control manifold was assembled with ¼ SS316 tubing rated to 5100 psi with the various components mounted to a laser cut acrylic backboard. Originally a manual pressure regulator was used to control the process gas, however this was upgraded to an electronically controlled regulator. This allowed for more precise tuning of the process pressure, as well as automation through an RS232-USB interface. The Equilibar EPR-3000 also features a self-contained vent mechanism which further reduced the demands on the operator. The assembled manifold is shown in Figure 15. The mandifold also has the general right-to-left flow structure where the HTHP Cell is out-of-frame to the left.

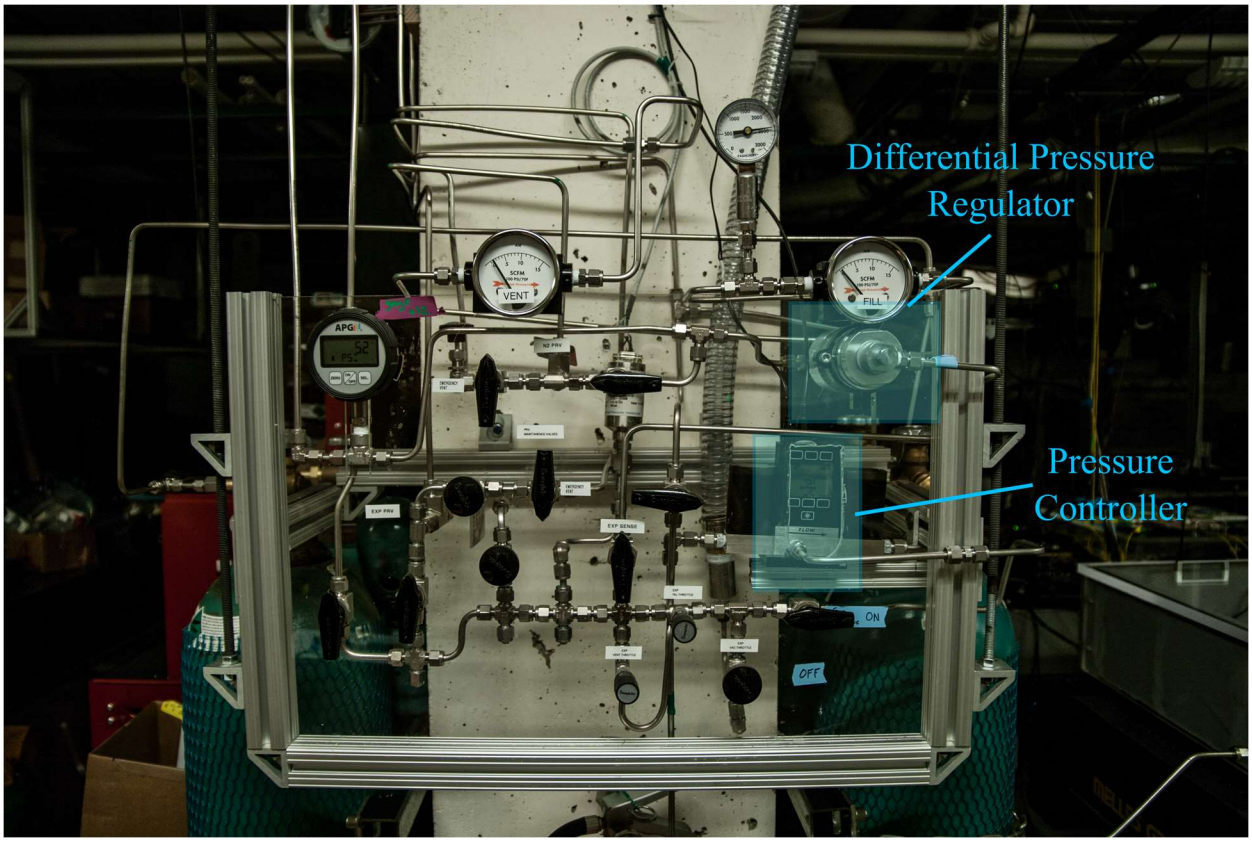

Fig. 15. Assembled gas handling manifold. The differential pressure regulator and electronic experimental gas pressure controller are indicated by blue boxes. The pressure vessel is out-of-frame to the left. Argon k-bottles are shown secured to the concrete column with the manifold.

4.2.3. Quartz Spectroscopic Cells

At the core of the HTHP Cell system are the quartz spectroscopic cells. As alluded to in Chapter 1, the dual-comb spectrometer has a nonlinear intensity profile that must be removed from the collected spectra by fitting a non-absorbing baseline. Generally with high SNR spectra, the baseline can be removed through a polynomial fitting routine, however for creating spectral databases an additional beam that recovers the baseline allows for improved spectral accuracy [52]. As such, the combined dual-comb spectrometer output is split into two identical beams that travel through the same optics, while only the experimental beam experiences the absorbing gas.

Measuring both signals at the same time then allows for the baseline to be precisely removed in post-processing. Originally an outboard window design with 3° wedges was chosen that permitted both beams to pass parallel to each other, however this design was quickly discarded. This original design is shown in Figure 16 with an UltraTorr Swagelok fitting at the end of the feedline that connects to the gas handling system.

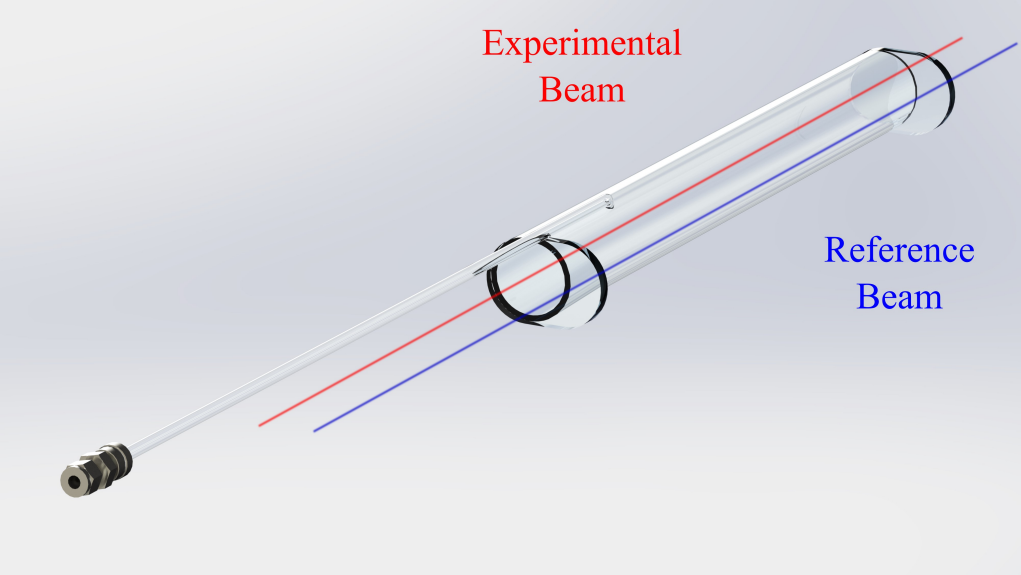

Fig. 16. CAD render of original outboard quartz spectroscopic cell design. The red experimental beam intersects the gas sample, while the blue reference beam only intersects the outboard windows. A feedtube is seen protruding from the cell with a Swagelok interface fitting attached.

It was discovered from manufacturers that the outboard section of the windows would likely become warped and obscured from sealing the windows to the quartz tube with a blow torch. Instead, a double-barreled design was chosen so that two tubes are arranged side-by-side with 3° wedged windows embedded within quartz tubes, as shown in Figure 17.

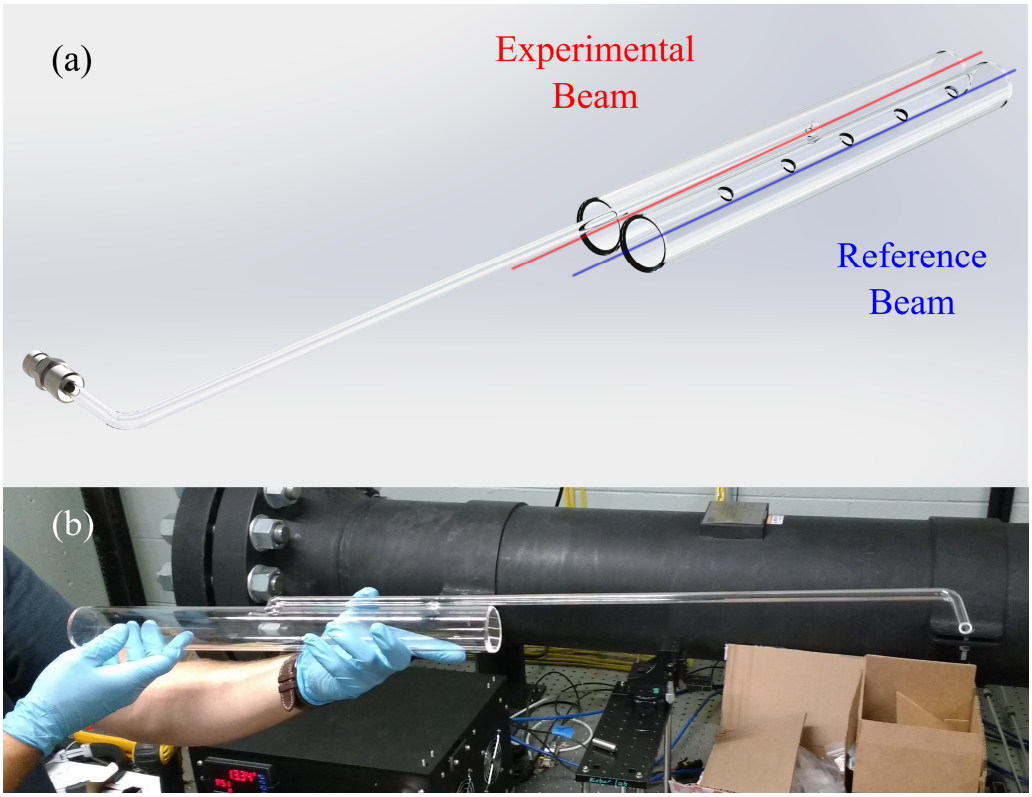

Fig. 17. Current quartz cell design. (a) shows a rendered CAD model with the experimental cell and beam in red, with the adjacent reference cell with the blue reference beam. The reference cell has holes to allow inert gas to easily flow through. The feedtube is noted to be bent at a 90° angle for the connection to the gas handling system. (b) shows the physical experimental cell being held for scale. 3° quartz windows are embedded in each side of the quartz tube.

The reference cell on the right is noted to have five holes through the midsection. This is to allow the bath gas to properly diffuse through the system allowing consistent temperature across the beam path. The experimental feedtube is attached at the center of the spectroscopic cell, extends outward, and then bends at 90° to allow connection to the gas handling system. A small glass support is also welded toward the end of the experimental quartz cell to secure the long feedtube. This also has the additional benefit of creating a known breakpoint if the bending stress becomes too much. Repairing a break during the straight portion of the feedtube would be much easier and cheaper.

The connection between the glass feedtube and the metal gas handling system is critical to maintain separation between the process and bath gases. Should this seal fail, the spectroscopic experiment would be ruined as the bath gas dilutes the experimental mixture. A Swagelok UltraTorr fitting with high temperature Viton o-rings was chosen after design consultation with Swagelok. This type of fitting is commonly utilized in vacuum systems, thereby indicating that the fitting should seal against a differential pressure of roughly 1 atm. However, the Viton creates a temperature limit of 150 °C as the elastomer loses rigidity, and while submerged in gases mearly inches from 1000 K a cooling solution was required. Additionally, the installation process necessitates a flexible solution to allow for feasible connection of the ends by an operator.

The small perpendicular access port only offers an inner diameter of 2.3 inches by roughly 7 inches in depth. Corrugated tubbing with welded tube ends allows for connection margin by coiling the tubing within the access port. As the port flange is installed with the corrugated tubing already attached, the coiled end is grasped within the main chamber of the pressure vessel and attached to the quartz feedtube through the UltraTorr fitting.

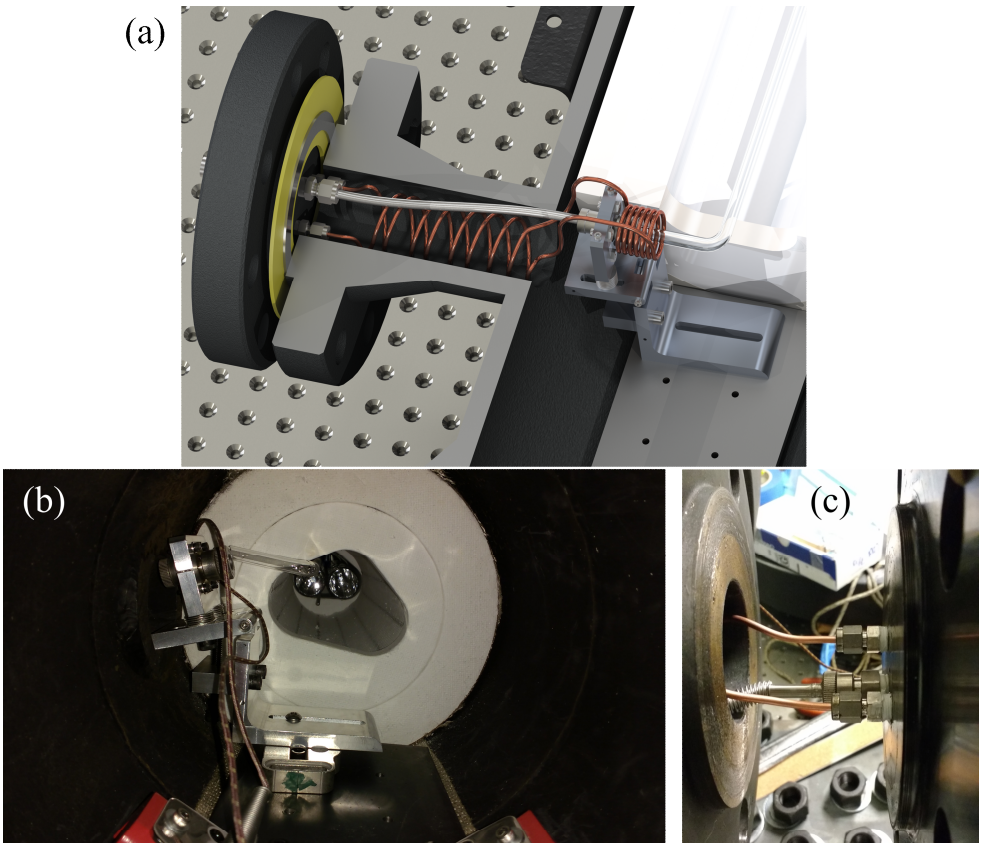

Fig. 18. Views of the gas handling connection to the experimental quartz cell. (a) CAD model rendering of a cross sectional view. A copper cooling loop is coiled within the access port, and then bent over and tighter around the Ultratorr Swagelok fitting. This keeps the Viton® seal within the design temperature limit, and a thermocouple is connected for monitoring. A metal slide assembly secures the fitting in place while connecting the gas handling system. Corrugated tubing makes the connection between the access port flange and the Ultratorr fitting, and is modeled as straight whereas is actually coiled inside the large copper cooling loop. (b) View through the right end of the pressure vessel with the feedtube disconnected from the fitting. The quartz spectroscopic cell are held in the middle of the 6 kW furnace. Thermocouple leads are also noted to be travelling between the furnace and pressure vessel wall awaiting installation. (c) Closing the access port flange with cooling loop and experimental gas line connected.

A 1/8 in copper tubing cooling loop concept was also created that wraps around both the corrugated tubing and UltraTorr fitting. As this connection is experiment-critical, a dedicated thermocouple is affixed to the fitting before sealing the system. A comparison of the modeled interface with the assembled version is shown in Figure 18. Although the flexible corrugated tubing is not modeled to the correct length, in actuality it is coiled inside of the copper cooling

loop. Considering the 24 cm ID clearance of the pressure vessel, this connection is troublesome to secure correctly to the feedtube without fracturing.

Optical simulations were also performed in Zemax, which is an optical system optimization and ray tracing software. The dual-comb spectrometer output was modeled in the physical system layout from the beam collimators, and the two beams propagated through the windows and quartz cells. A detector area was modeled on the receiving end of the system, and variations in the input beam pointing were tested. For each set of these input parameters the ability of the beam to hit the detector is tested. This verified that the cell orientations were feasible for the beam to pass through the entire optical system. From this analysis, it was found that the system was easily feasible and the exterior sapphire windows largely contribute to the optical stability.

4.2.4. Furnace and Electrical Control

As mentioned in the previous section, the furnace power is supplied through three 8 AWG magnetic wires housed within a high performance feedthrough, which is in addition to 20 type-K thermocouple wires through similar feedthroughs. The feedthroughs are shown installed on the leftmost flange in Figure 19.

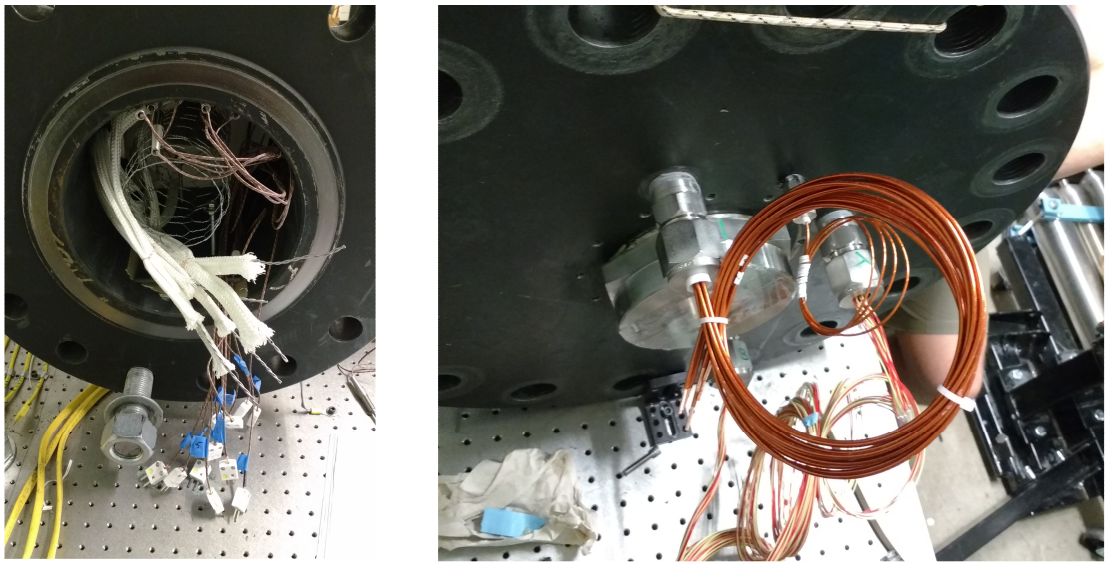

(a) (b)

Fig. 19. Power-side outer flange with electrical connections. (a) Pressure vessel with furnace and thermocouple leads exposed awaiting installation. A wire mesh assembly is held in the center of the pressure vessel to keep wires from interfering with the optical path. (b) Ambient-facing side of power-side outer flange with feedthroughs and window installed. Power feedthrough is installed closest to camera and, moving clockwise, the ground and two thermocouple feedthroughs are seen.

The thermocouple leads on the exterior of the vessel are directed to a centralized data collection box that displays the readings, and communicates them to the main data acquisition computer. This collection box also contains a transducer reader for the process pressure, and safety mechanisms to cut furnace power and halt system operation. These safety mechanisms are connected to the respective outputs of the pressure and temperature readers and are programmed to de-energize input power relays thereby halting the system operation. The transducer measurements can then be assessed visually via the readouts, but are also fed into the data acquisition computer over USB and RS232-USB interfaces. In total, an original ten internal thermocouples were utilized, with five exterior sensors, and their locations are shown in Figure 20.

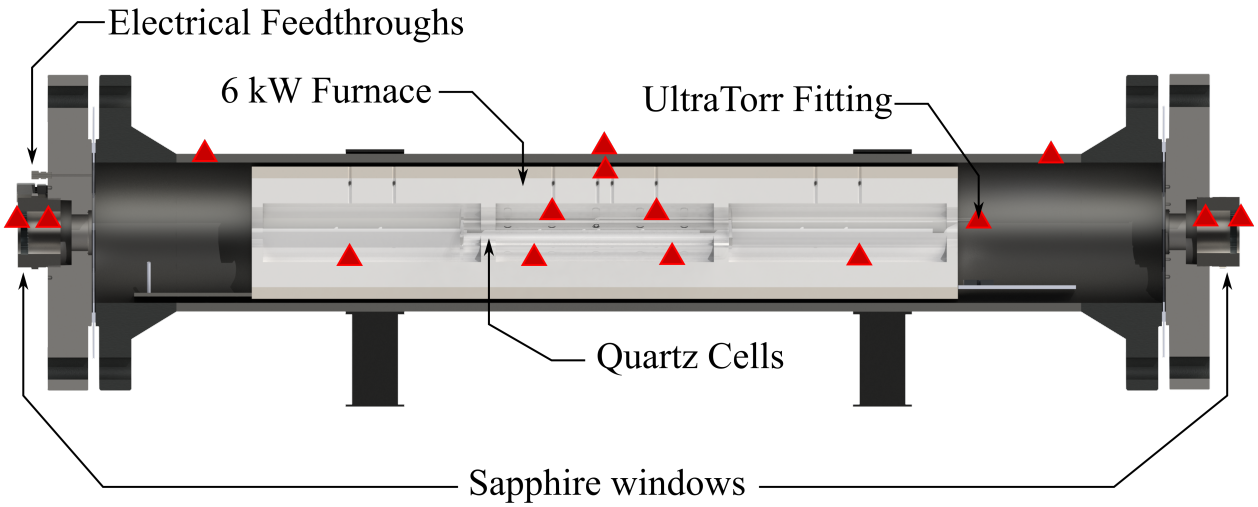

Fig. 20. CAD model cross sectional rendering showing thermocouple locations with red triangles for 6 kW furnace. Five thermocouples have locations on the exterior, while the others were inside.

Temperature tests were conducted which revealed a pressure dependence on the temperature uniformity and pressure vessel external temperature distribution. As the pressure was increased, the temperature uniformity within the furnace degraded by roughly 0.3 K/psi for a standard deviation of approximately 60 K at 12.5 atm. Additionally, hotspots were noticed on either end of the pressure vessel correlating with the large open volumes as shown in Figure 20. From first order approximations, these hot spots were determined to be from convective heat transfer loops initialized by the introduced bath gas. During a test an element of the 6 kW furnace burned out which necessitated a redesign with a new furnace. This test is discussed in further detail in the Appendix.

The new furnace was fabricated by DelTech Furnaces that utilizes SiC rods and a phase-current controller to obtain the desired temperatures. This design was closely related to the one utilized within the Colorado School of Mines gasifier, as they conveyed the robustness and ease

of maintainence of their system [53]. A side view of the acquired SiC furnace is shown in Figure 21.

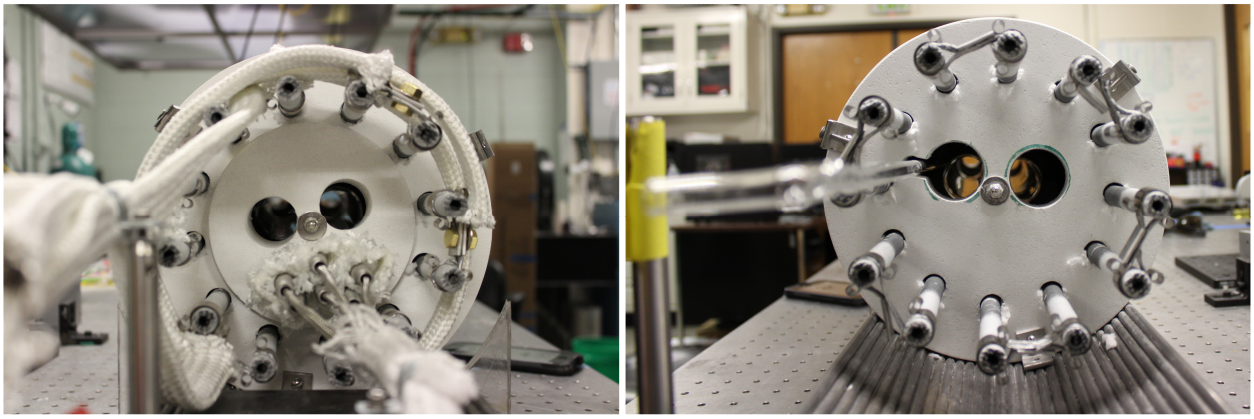

(a) (b)

Fig. 21. New SiC carbide furnace. (a) Power-side view with 3-phase delta connection to SiC rods toward top of furnace, and thermocouple leads in bundle toward bottom. (b) Gas-side view of the furnace. The quartz feedtube from the experimental cell is seen protruding toward camera and left.

Around the exterior of the furnace are 102 cm long hollow SiC rods, 1.3 cm OD, which are connected for three-phase power at 480 VAC for a total of 17 kW available heating. Should a SiC rod burnout, the rod simply needs to be disconnected from the array, removed, and a new rod installed. There are also ceramic endcaps with two side-by-side holes that permit laser light to each of the quartz cells. The endcaps also help to retain the hot furnace gases within the furnace volume, and helps to reduce convective currents from creating hotspots on either free volumes of the pressure vessel.

In addition to the new furnace, the data acquisition process was improved. Within the main data acquisition computer, various Python scripts were ran that automatically collect data, and saved the data to InfluxDB databases through a locally instantiated InfluxDB server [54].

InfluxDB was chosen as the time-series database due to its ability to high data compressibility potential and its fast query speeds [55]. The InfluxDB database shards were also stored within a Google Drive folder which maintained data backups regularly. A server instance of Grafana was also run locally on the data acquisition computer that allows an operator to quickly assemble dashboards and assess system performance from anywhere on the local network [56]. An example of such a dashboard is shown below in Figure 22.

Fig. 22. Grafana dashboard displaying temperature readings. Moving clockwise from the top-left the graphs are displaying: power-side window temperatures, gas-side window temperatures, skin temperatures, and the Ultratorr temperature. Interior is denoted as red while exterior is yellow. The Ultratorr does not a color scheme as it is a single location. Design limitations are set in horizontal yellow lines corresponding to 10 °C from the limit, and horizontal red as the design limitation.

The Grafana server was linked to the InfluxDB query port and custom graphs were created for the thermocouple, pressure, and detector readings. Alerts were also set for the different measurements to signal when certain readings were too close or exceeding their design limit. Three dashboards were subsequently created for the different system metrics: pressure control, process temperatures, and overall temperature readings. The temperature readings also

provided a nearly direct measure of performance of the furnace, and indicated where certain hotspots were located. Software meant to monitor and control the furnace power loading also gave measures of the furnace duty cycle as well as the direct amperages being utilized.

4.2.5. Exterior Windows

In addition to the exterior pressure vessel, there must be optical access to the system which also experiences the full design pressure. This optical window must be exceptionally strong to hold back the interior 100 atm along with withstanding the increased temperatures. There are generally two window design methodologies for pressure and vacuum vessels: unclamped and fully clamped, as shown in Figure 23. The unclamped method induces higher stresses upon the window, and if possible the fully clamped design is preferred.

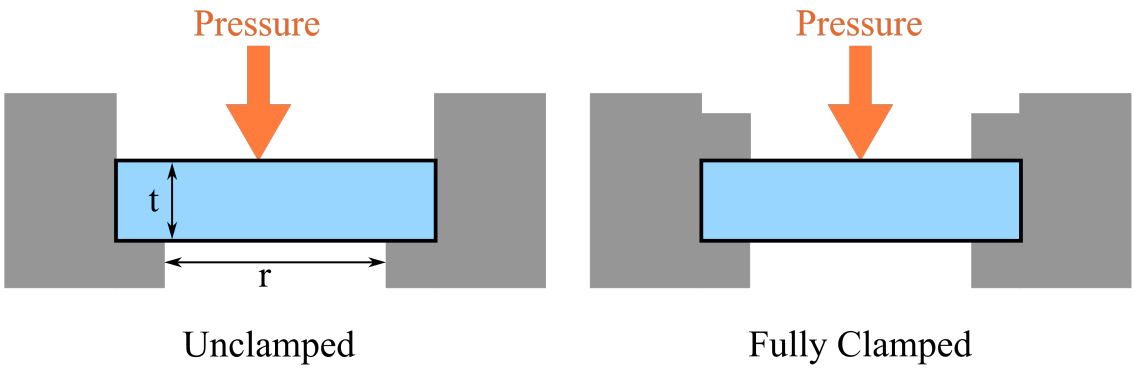

Fig. 23. Diagram showing pressure vessel, or vacuum vessel, window clamping methodologies.

The required thickness for a high pressure window is calculated for a circular edge-clamped window using Eq (4.1) from Advanced Glass Industries where r is the unsupported window radius, P is the pressure differential across the window, K is a geometrical constant of 0.75, FoS is the factor of safety, and M is the modulus of rupture [56,57] . For an unclamped

edge the geometrical constant is 1.125. Eq (4.1) is also not valid for rectangular windows. The radius of the windows was chosen to be 6.35 cm, excluding clamping, to have the largest feasible area for the laser beams without requiring an exorbitant thickness.

$$t = r\sqrt{\frac{P \cdot K \cdot FoS}{M}} \qquad (4.1)$$

This equation was validated by derivation from deflection formulas for ideal beams with clamped ends. The necessary thickness for a fully clamped circular window with a factor of safety of 4, and unsupported radius of 2.86 cm for various optical materials was calculated and is shown in Table 1.

Material	**Modulus of Rupture**	**Required Thickness at $FoS = 4$ [cm]**
BK-7	2400 psi, T = 298 K	4.29
Fused Silica	7600 psi, T = 298 K	2.41
Zinc Sulfide	15,900 psi, T = 298 K	1.68
Sapphire	60,916 psi, T = 293 K	0.86
	40,610 psi, T = 773 K	1.04

Table 1. Required window thickness based on modulus of rupture for design pressure [56,57].

Clearly sapphire gives the best mechanical performance, and a thickness corresponding to the average temperature was chosen as 0.94 cm, thereby creating a design limitation of 533 K. However, an issue prevalent in absorption spectroscopy that must be taken into account is that of etalons. Etalons arise when an incident beam refracts inside a material of differing index of refraction To overcome this, a 3° wedge was also applied to the window to which gave a maximum thickness of 1.35 cm. The transmission spectrum, shown in Figure 24, also

demonstrates that sapphire is well-suited for the system with nearly 90% trasmittance between 1 and 2 µm.

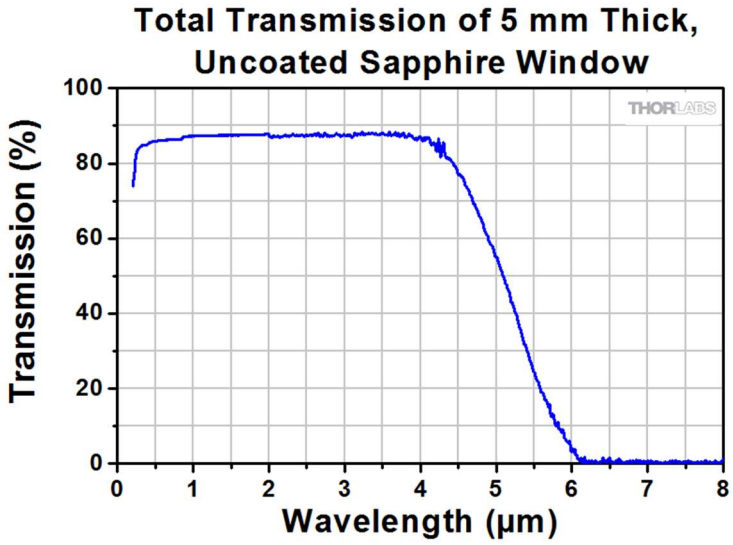

Fig. 24. IR transmission spectrum for 5 mm sapphire [57].

The original window assembly was designed with a recessed cavity into the outer pressure vessel flanges, with a retaining ring applying the necessary preloading before pressurization. Due to the high temperatures and pressure that may be encountered by the sealing interface, various sealing mechanisms were explored. While an elastomeric seal, such as Viton® or Kalrez®, gives good high temperature performance these materials are typically limited in operation up to 220 °C and would consume a large amount of space from the outer flange. Instead, an Inconel 718 c-seal from Jetseal was utilized due to its superior temperature and pressure performance as well as the elimation of the possibility of seal blowout. Shown in Figure 25 is a cross sectional view of the sapphire window retaining mechanism.

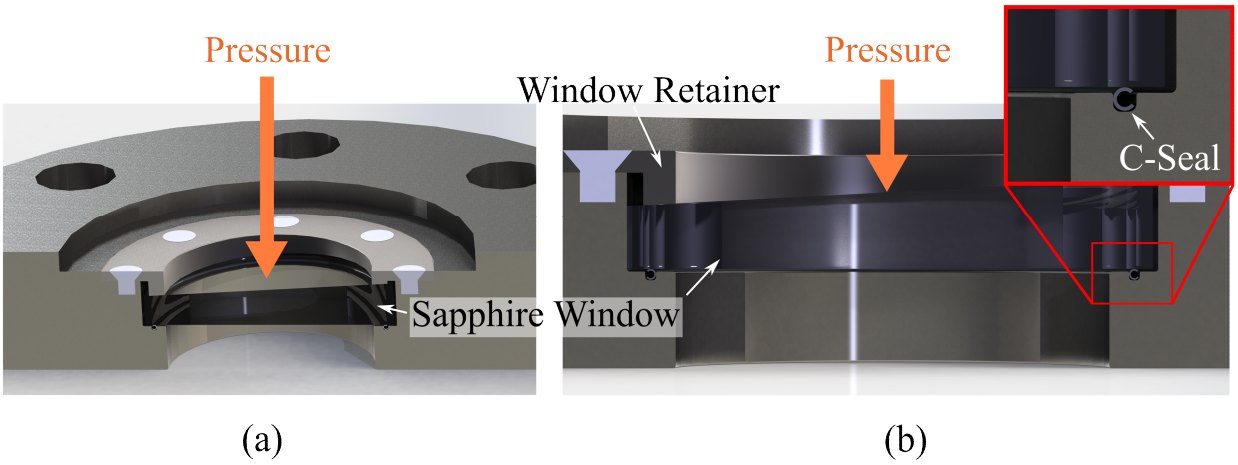

Fig. 25. Cross sectional view of previous sapphire window retainer mechanism. Internal presure forces the window into an Inconel 718, silver-coated, c-seal while a SS304 retainer provides preloading.

The c-seal operates on the principle that the interior of a 'C' faces the sealing pressure, thereby pushing one side of the seal into the sapphire and the other into the groove material. A retaining ring with eight 1/4-20 bolts was designed and fabricated through an external machining company. This design requires only 0.13 cm of groove depth for the seal and 6.78 N-m torque per bolt.

However, a window failure occurred during the first hydrostatic test of the system that catalyzed a design change. The sapphire windows were installed into the modified outer flanges, the retainer secured to the proper torque, and a fiberglass material was placed between the sapphire and retainer. The outer flanges were then installed onto the main pressure vessel and the bolts tightened. The pressure vessel was then filled with water from the laboratory cold-water supply, and a pressure applied with gaseous N_2 in steps of 100 psi until a final pressure of 2000 psi. During each step the system was inspected for leaks, and roughly 10 min after the system reached 2000 psi water was noticed to be pooling around one of the flanges. Upon closer

inspection it was discovered that a fracture had occurred in the window, but that the window had managed to retain the water pressure without complete failure. Shown in Figure 26 are views of this fracture.

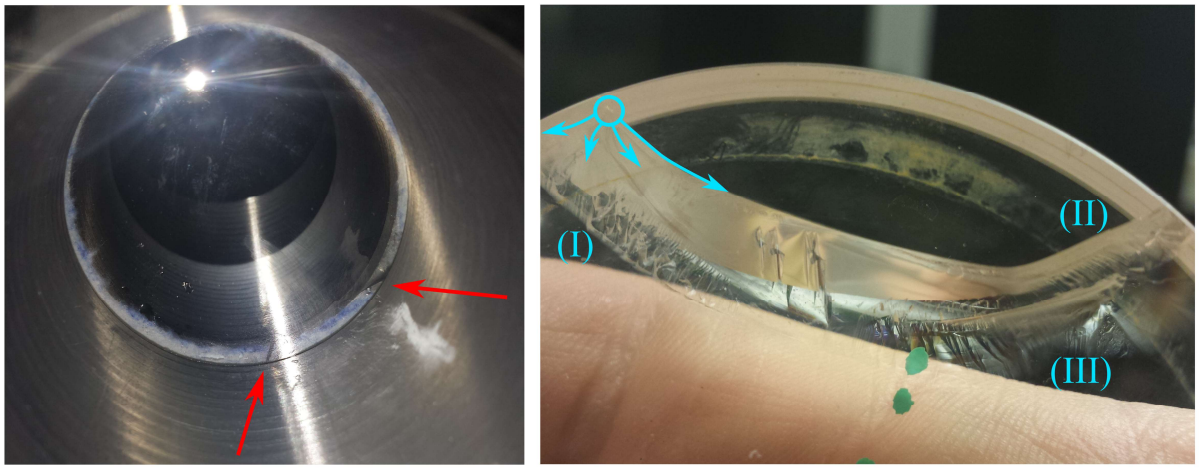

(a) (b)

Fig. 26. Sapphire window fracture. (a) shows the sapphire with fracture locations indicated by red arrows. (b) is a closer view of the sapphire from the pressure side, with likely fracture initiation point indicated by the blue circle. The direction of fracture is indicated by the blue arrows. Region I indicates twist hackle marks where tensile stress titled from crack surface, along with mist hackle near the circle indicator. The fracture has penetrated through the sapphire at Region I. Region II has indications of Wallner lines, convex to the right, giving evidence that the crack propagated from left to right. Region III again showed evidence of twist hackle, however the fracture is noted to have not penetrated the full distance of the sapphire thickness.

Removing the sapphire window revealed that the fracture was only partially throughout the thickness of the sapphire, and closer insection of the fracture patterns yielded valuable information about the probable cause. Twist hackle marks were seen toward the high pressure side of the sapphire, indicating both tensile stress fracturing, as well as that the fracture moved from the ambient side to the high pressure side. Mist hackle was also seen to have been localized around the region indicated by the blue circle in Figure 26 (b), pointing to a likely origin point.

Toward the right of the sapphire, relative to Figure 26 (b), Wallner lines were noted to be convex to the right. This indicated that the crack moved from left to right. Furthermore, the sapphire fracture penetrated the full thickness in only the region that had the mist hackle marks.

It was concluded that imperfections in the surface quality of the gland recess created a stress concentration on the sapphire when the window retainer was torqued. By itself this did not cause failure, but perhaps at the final test pressure the sapphire slightly shifted due to an imbalance of force generated by the wedge. This slight movement likely caused a surface crack to form at the stress concentration, indicated by the blue circle in Figure 29 (b), and to propagate across the window from the bending moment. While only one of the two installed windows failed, this indicated too high of a failure sensitivity for a critical safety component. An external company specializing in sight windows for pressure vessels was consulted to design a more robust window system. Rayotek Sight Windows was chosen to design and manufacture a 4 in NPT fitting out of SS316 that housed the already purchased sapphire windows. A sealant is introduced between the sapphire and SS316 to retain the sapphire in place and to prevent leaks, however this again limits the operational temperature to 200 °C. The window fittings are then regarded as single components. The fittings are installed with a custom socket adapter as shown in Figure 27.

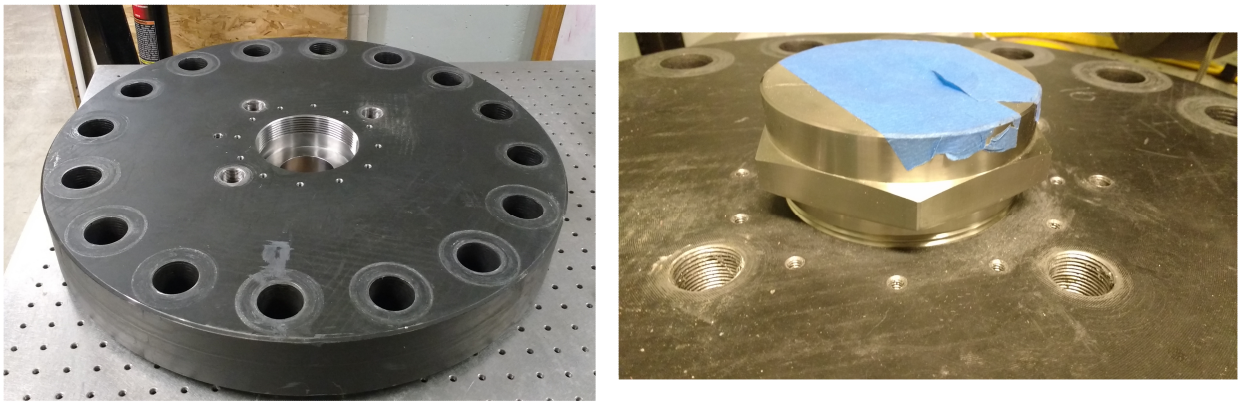

(a) (b)

Fig. 27. Sapphire window retainer installation on outer flange(s). (a) shows the power-side outer flange, as noted by the additional smaller NPT ports, with the large 4 in NPT port in the center. (b) is a window retainer installed into the outer flange. Blue tape is covering the exposed sapphire.

An anaerobic resin thread sealant is applied to Rayotek's specifications to the fitting threads before they are torqued into place. As part of the standard operating procedure, as shown in Figure 27 (b), the windows were also covered when not performing an experiment to help dissuade surface imperfections from forming. Lastly, they are also wrapped with ¼ in copper tubing connected to the cold water supply during operation to maintain temperature stability.

As the windows have the lowest factor of safety of the system, procedures and mechanisms were developed in order to ensure operator safety should they fail. The energy of a compressed gas was approximated by Eq. (4.2) from [58] which results from the thermodynamic availability within the gas.

$$E = P_2 V \left[\ln\left(\frac{P_2}{P_1}\right) - \left(1 - \frac{P_1}{P_2}\right) \right] \qquad (4.2)$$

Once the explosive energy of the gas was obtained, it was then converted to the equivalent mass of TNT using Eq. (4.3).

$$W = E \cdot \left(\frac{1 \text{ kg TNT}}{4.184 \times 10^6 \text{ J}} \right) \tag{4.3}$$

This value was then converted to a scaled distance using Eq. (4.4) to use prior relationships developed by various military agencies for blast conditions.

$$Z = \frac{R}{\sqrt[3]{W}} \tag{4.4}$$

Lastly, the simplified Kingery-Bulmash equation developed by Swisdak, shown in Eq. (4.5), was utilized to calculate the peak incident overpressure, P_s [59].

$$P_s = e^{(A+B\ln(Z)+C\ln^2(Z)+\cdots+G\ln^6(Z))} \tag{4.5}$$

The parameters for the Swisdak equation are listed in Table 2 [59].

Z [m/kg$^{1/3}$]	A	B	C	D	E	F	G
0.2 – 2.9	7.2106	-2.1069	-0.3229	0.1117	0.0685	0	0

Table 2. Swisdak equation coefficients for given scaled distance range.

The result of this analysis is shown in Figure 28 for the overpressure amount, as well as the corresponding sound level. The above equations were developed for surface blasts of equivalent TNT charges, which correspond to a higher overall peak pressure due to shockwave reflection from the ground. Typically the reflected pressure will be greater than the incident pressure calculated above, however the development of choked flow should a rupture occur will decrease the magnitude of shock effects. Additionally, the leak-before-break criterion of the pressure vessel reduces the likelihood of complete and total instantaneous gas release as again choked flow would again initialize upon the most probable failure mode of the pressure vessel.

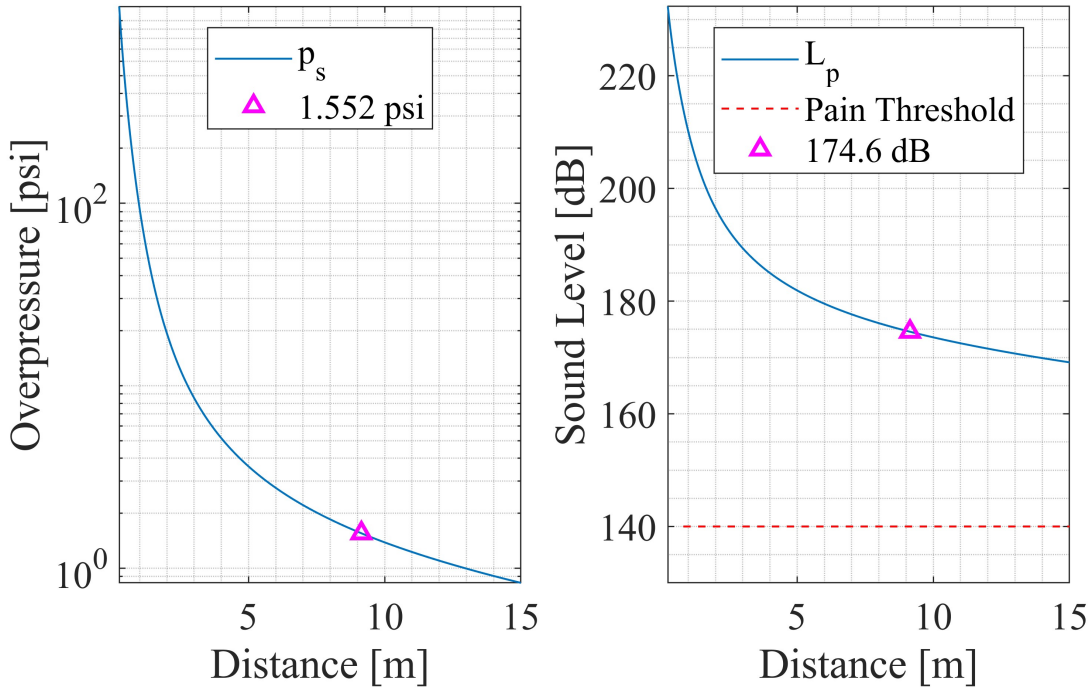

Fig. 28. Overpressure resulting from equivalent TNT for experimental compressed gas volume. Values of 1.552 psi overpressure and 174.6 dB indicated by magenta triangle corresponding to operator distance at edge of keepout zone. The calcualted sound level above the pain threshold indicates the necessity for permament forms of hearing protection to be worn at all times the vessel is pressurized.

The U.S. Department of Health and Human Services lists the auditory threshold of pain in humans as between 120-140 dB [60], necessitating two forms of over-the-ear hearing protection to be worn at all times in addition to safety glasses. Over-the-ear earmuffs were ordered which provide a nominal 29 dB noise reduction rating, and standard foam ear plugs were also mandated to be worn at all times which nominally provide a 28 dB noise reduction potential. Together these bring the sound level at the operator distance of 9.1 m to below the threshold of pain. It was also found by the U.S. Department of Defense and U.S. Department of Energy reports that a 5 psi overpressure caused eardrum rupture in 1% of subjects [61]. From the analysis it was concluded that a strict 9.1 m keepout radius be enforced during operation, and

that the laboratory be vacant besides essential personnel. This analysis also accelerated automation design choices to reduce interaction time of the operator in the laboratory during experiments. This brief analysis is also not meant to serve as the safety standard, but to provide estimates for potential failure modes. These estimates are then meant to provoke further analysis such that additionaly safety measures may be implemented. Considering the potential for harm, safety mechanisms should not only implemented through passive methods but also with active methods, including the culture of operation. Multiple layers of protection need to be properly executed for operator safety, but the system needs to be designed with enough failure tolerance to keep the operator safe regardless of if those mechanisms should also fail. Besides the hazards associated with the compressed gas, potential shrapnel effects were also considered if the windows were to fail.

The Bird, Steward and Lightfoot source model, shown in Eq, 4.6, describes the time to exhaust a gas for an accidental release of a pressurized vessel assuming choked flow [62]. Within Eq. 4.6, γ is the specific heat ratio, F is the fraction of gas remaining in the vessel, V is the vessel volume, C_V is the coefficient of discharge, P_0 is the original vessel pressure, and ρ_0 is the original gas density within the vessel.

$$t = \left[F^{(1-\gamma)/2} - 1\right]\left(\frac{2}{\gamma - 1}\right)\left(\frac{V}{C_V A}\right)\sqrt{\frac{\gamma P_0}{\rho_0}\left(\frac{2}{\gamma + 1}\right)^{(\gamma+1)/(\gamma-1)}}$$

$$F = \left\{t\left(\frac{2}{\gamma - 1}\right)\left(\frac{V}{C_V A}\right)\sqrt{\frac{\gamma P_0}{\rho_0}\left(\frac{2}{\gamma + 1}\right)^{(\gamma+1)/(\gamma-1)}} + 1\right\}^{2/(1+\gamma)} \qquad (4.6)$$

The source model was rearranged to give the fraction of gas mass remaining within the vessel at a given time t. The pressure and temperature as a function of time can then be calculated through isentropic relations as Eq. 4.7.

$$P(t) = P_0 F(t)^{\gamma}$$
$$T(t) = T_0 F(t)^{(\gamma-1)} \qquad (4.7)$$

This was utilized in combination with kinematic equations to determine the velocity of the sapphire through numerical integration. Assuming an unrealistic, although upperbound, situation of the entire window exiting the window retainer as a single piece with a constant initial velocity of 210 m/s, the impact dynamics were assessed. An explicit dynamics simulation was performed with Autodyn as part of ANSYS® 16.0, with the results shown in Figure 29 [63].

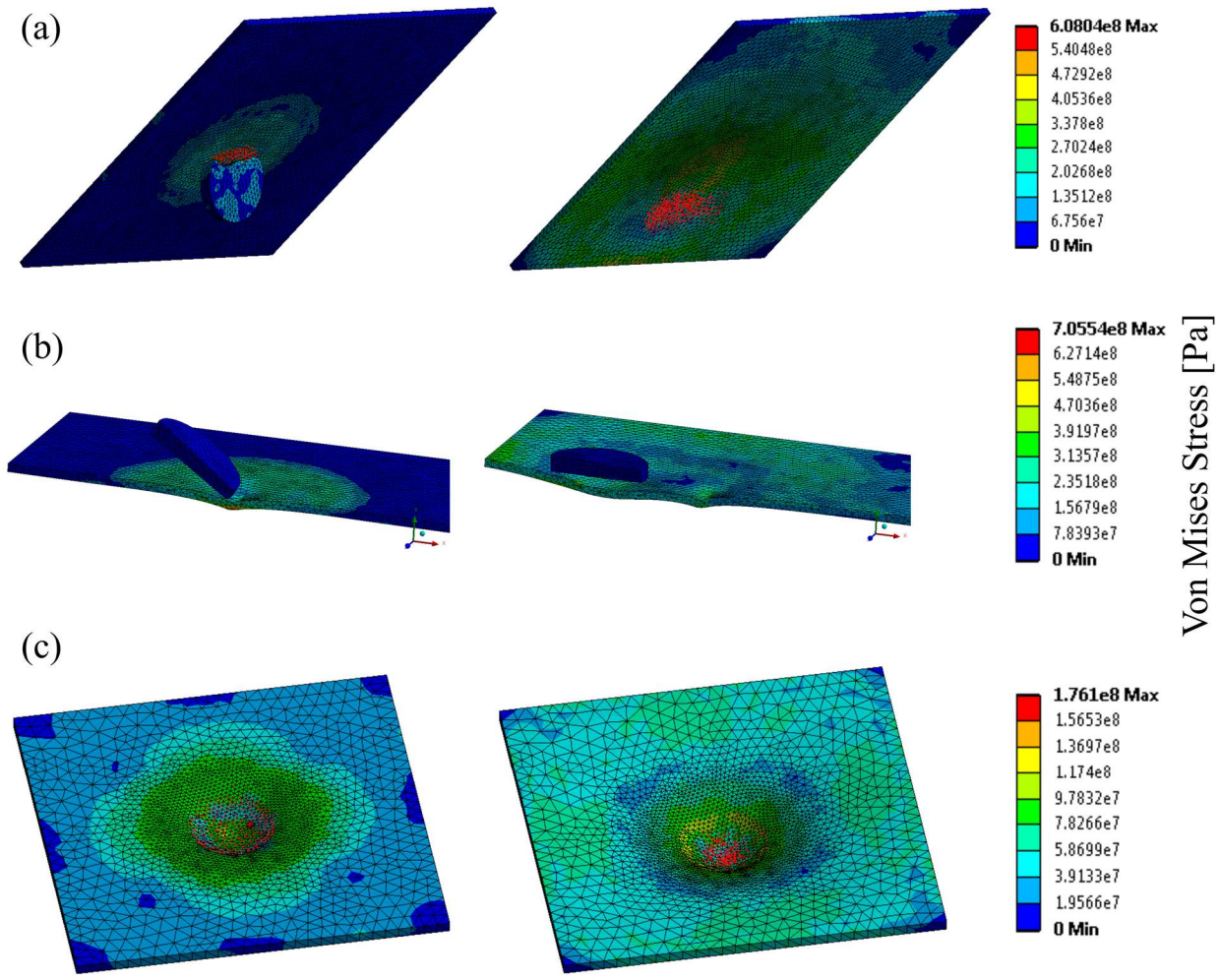

Fig. 29. Explicit dynamic simulations of whole sapphire impacting 1/4 in steel plate at 210 m/s in different orientations. (a) shows sapphire window impacting at 45°, and with complete sapphire window failure. Permanent deformation of the steel plate is noted, however no penetration. (b) is the same 45° orientation, however the sapphire is modelled as rigid with the same original density. A larger deformation is noted, but no penetration of the plate is observed. Spalding resulting from tensile failure on backside of plate is predicted to occur. (c) face-on, i.e. flat edge of sapphire window parallel to steel plate, impact. This orientation exhibits the highest deformation along with complete failure of the sapphire window. Stress is distributed across plate and no failure of the steel plate is predicted.

A rigid edge-supported 0.64 cm steel plate was impacted with the sapphire at an angle of 45° showing complete fracture of the sapphire and a downward momentum carrying the shrapnel pieces. The steel plate performance was also assessed by assuming that the sapphire window was

rigid and would not fracture, although it had the same density. This resulted in two large indentations of the steel, but did not penetrate the plate. However, the impact resulted in spalding of the backside of the plate from tensile failure, but not complete failure of the plate. Lastly, a face-on collision was also assessed. From this analysis it was concluded that a strict keepout zone down range of the windows be enforced during pressurized operation of the HTHP Cell. Additionally, two blast shields were welded that included a 0.95 cm steel plate reflector. This reflector is angled such that should a window failure occur, the shards would be directed downward into a steel box enclosure to contain any potential shrapnel. These were subsequently bolted to the optical table with four 1/4-20 steel bolts each.

4.3. System Overview

Putting together the individual system components allows for the overall system viewpoint to be developed. A top-down cross sectional view of the system displaying the optical pathways is shown in Figure 30.

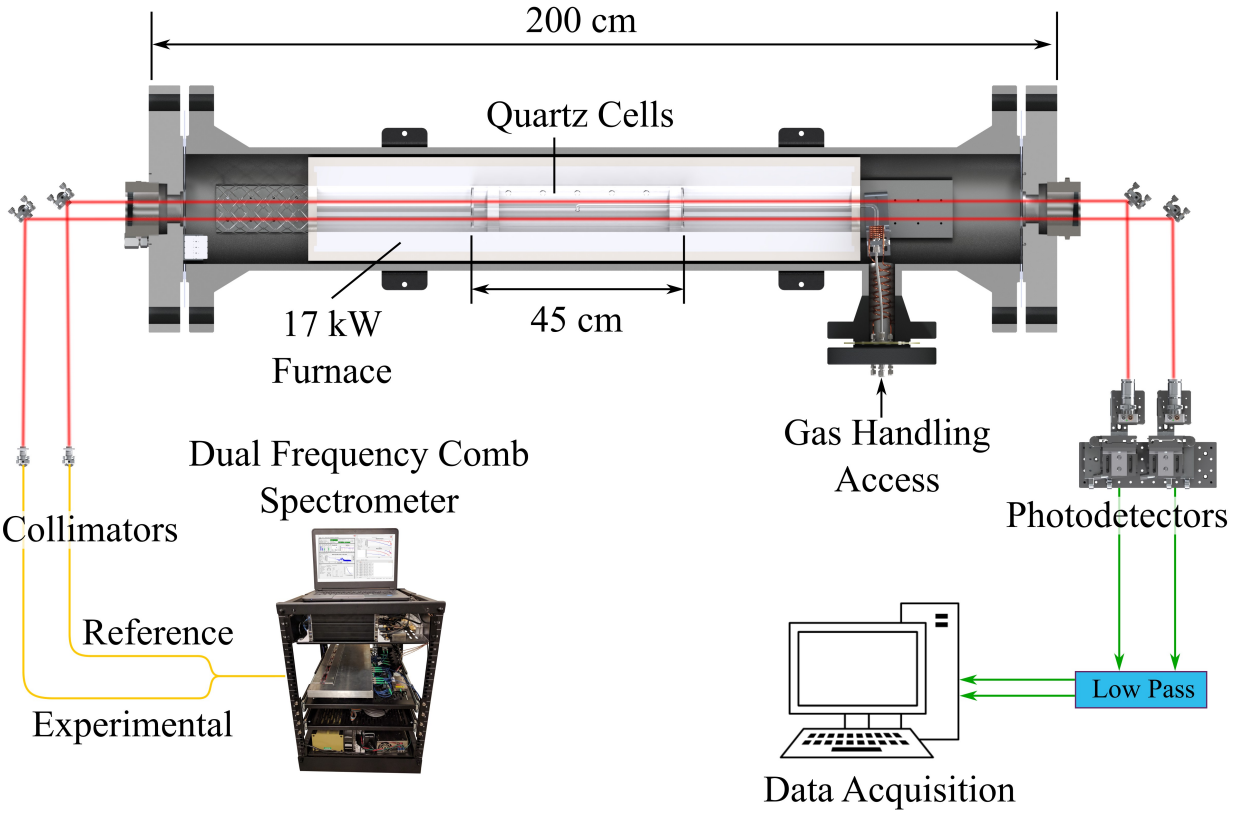

Fig. 30. Top-down cross section optical setup. The dual-comb spectrometer heterodyned output is split into the reference and experimental fibers, which are fed to fiberized collimators. These beams travel parallel to each other; one through the reference cell and one through the experimental cell. They are received by two mirrors outside of the pressure vessel which direct them into fast photodetectors. The photodetector signals are low-pass filtered, the DC component removed, and given to the data acquisition system.

The two comb outputs of the dual-comb spectrometer are combined and then split into two identical beams that are collimated through 90° off-axis parabolic mirrors (Thorlabs RC02FC-P01). The beams are then reflected off of two 1 in diameter silver mirrors, passed through the HTHP Cell, and lastly reflected off another two 1 in mirrors into focusing lenses and the fast photodetectors (Thorlabs PDA10CF). While the system is unpressurized, the furnace is brought to the desired setpoint and allowed to reach steady state. A HeNe laser at 632 nm, the red portion of the visible spectrum, is first connected to the fiberized input of the collimators to

allow for relatively easy alignment of the optics. Near-IR comb light is then connected from the dual-comb spectrometer through single mode fiber. IR cards are utilized to verify and hone the laser path to successfully be collected by the photodetectors. The DC component of the detector signal is split with a bias tee and provides a measure of how well the beam is aligned. This voltage is maximized by adjusting the mirror tip-tilt axes, as well as the collimators, to finish the alignment before an experiment. The collimators additionally have piezoelectric tip-tilt motors (Thorlabs PIAK10) that allow for remote control alignment while the system is at elevated pressure. The fully assempled HTHP Cell during the beginning of an experiment is shown on its 4.27 m optical table in Figure 31.

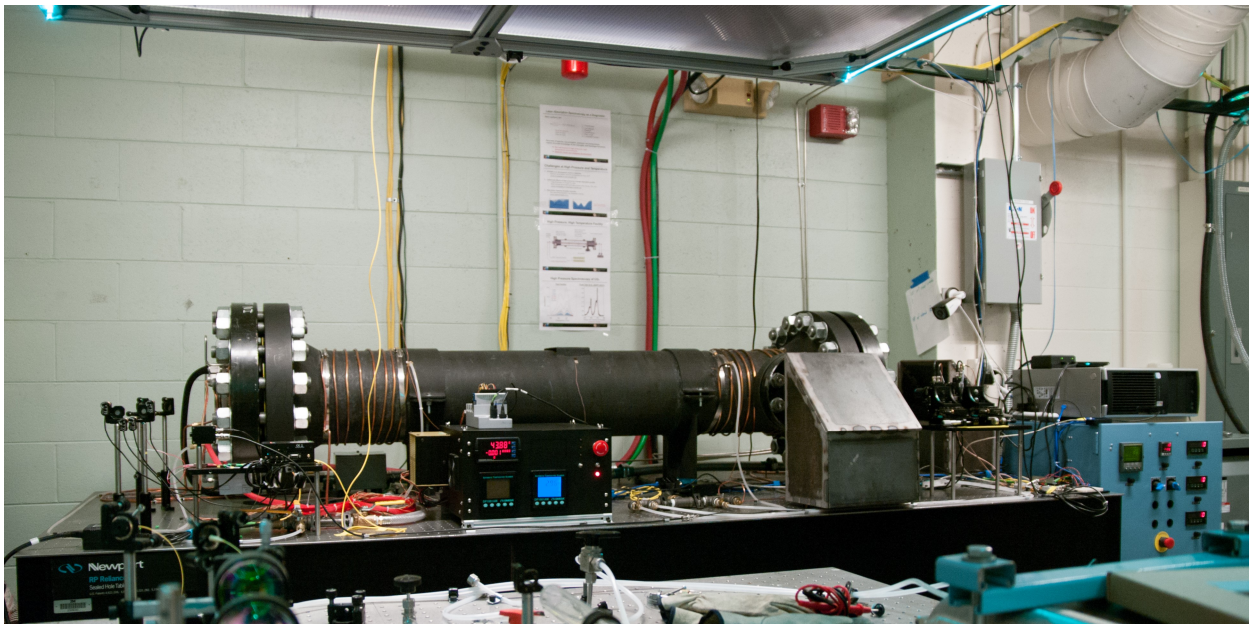

Fig. 31. View of HTHP Cell during data collection in June 2018. The electrical box containing sensor readers is in the middle of the image, toward the left of the optical table, with red LCD text showing the process pressure reading. A blast shield is installed in front of the access port flange, and out-of-frame to the left of the image is a 61 cm thick concrete wall. The furnace power controller is to the right of the image in blue, showing the duty cycles of the three 480 VAC phases.

As with all real-world experiments hurdles are encountered that need to be circumvented. During testing thermal control issues arose, and necessitated internal and external thermal control measures that drove design improvements. Despite these setbacks, high quality data was collected during June-July 2017 and June-July 2018. Typically characterization tests were combined with spectral data collection as operation of the HTHP Cell requires two-person operation across a few days, as well as multiple day setup time allocation.

4.4. System Performance

4.4.1. Ability to achieve high temperature and high pressure

Performance characterization testing was performed while also taking spectroscopic measurements of high-temperature, high-pressure, CO_2 in July 2017 and June 2018. The first datarun did not have the complete automated data acquisition system installed, and so a history of pressure is not available, and the temperature data available is sparse. Due to these factors, those data will not be discussed here.

The second collection campaign over June 2018 yielded much higher quality system characterization data as the effects of temperature and pressure were better observed with continuous logging. Multiple temperatures, process pressure, and photodetector voltages were logged which allowed a timeseries snapshot of how the system interacted, which is shown in Figure 32.

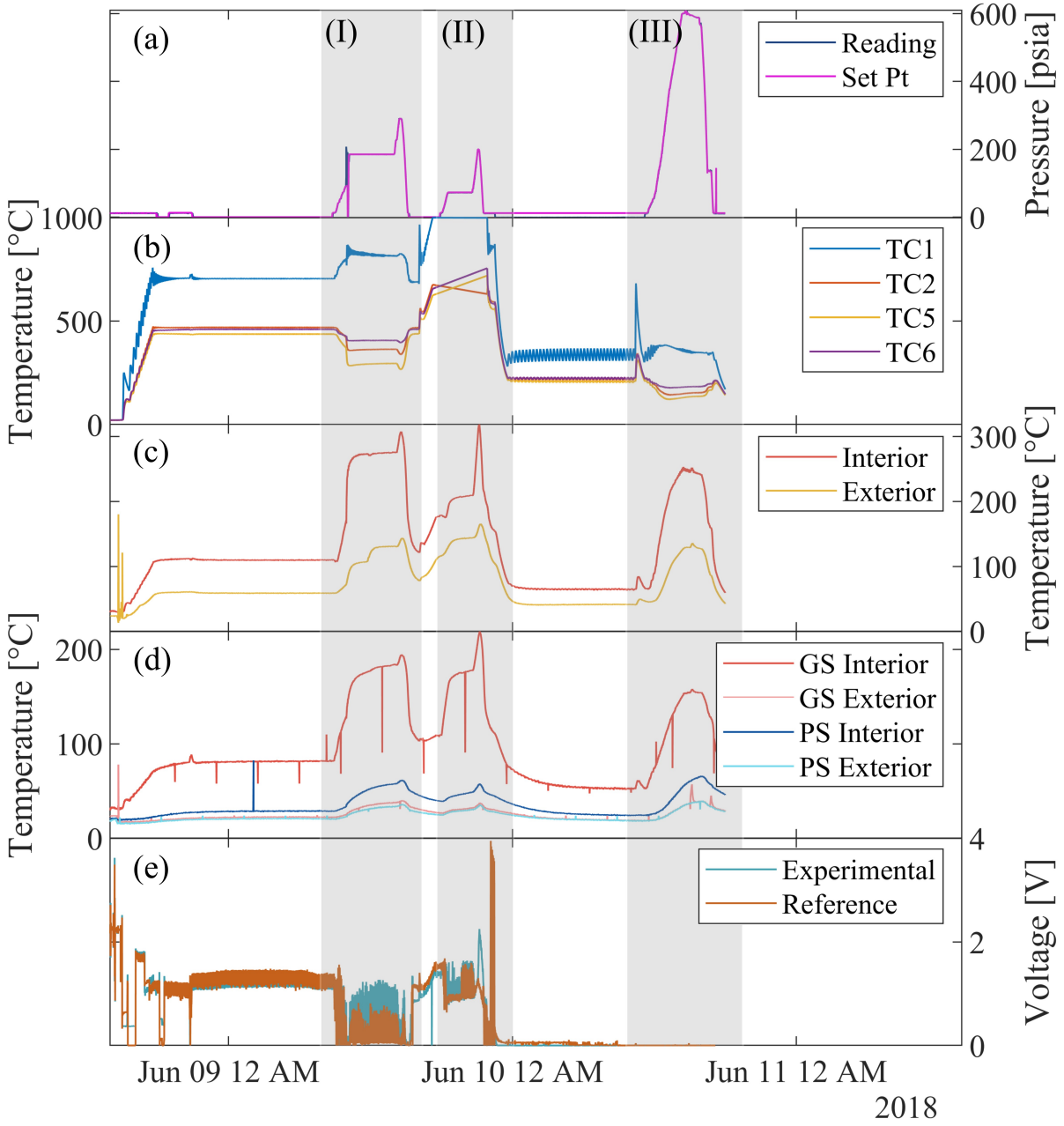

Fig. 32. HTHP Cell metric readings during multiple data collections in June 2018. From top-to-bottom the graphs show: (a) process pressure, (b) process thermocouples, (c) center skin temperatures of prsesure vessel, (d) gas-side (GS) and power-side (PS) sapphire window temperatures, and (e) DC component of detector voltages.Region I marks the two data collections, and demonstrates the effects of pressure on optical alignment. Region II contains more data collection, but electrical issues caused the process thermocouple readings to be lost. Region III contains system performance testing without data collection, hence near-zero detector voltages.

From mid-day June 8th to end-of-day June 10th three tests were performed, as indicated by Region I, II, and III in Figure 32. Only Region I will be discussed here as similar trends are noted across the regions. The curious reader is directed to the Appendix for discussion of the other two regions, along with a diagram showing the thermocouple locations. Prior to these tests, spectra were also collected at 1, 3, and 7 bar, however the data collection system was not fully developed excluding system characterization data from those collections. Region I consisted of spectra collection at 13 bar at approximately 750 K spanning a few hours. This was followed by increasing the pressure to roughly 20 bar and collecting half an hour of data, and subsequently depressurizing the HTHP Cell until the bath gas was equal to the ambient pressure. The quartz process cell was vacuumed, and the furnace commanded to a higher temperature. Unfortunately, during this time, the data acquisition system experienced an error which corrupted the data. The thermocouple reader was functioning properly, however, and so the operators were still able to visually determine the health of the system. After the furnace temperature was increased, gas was added to the system to bring the pressure to 7 bar. Data was collected and then another pressure increase was performed. However, as more gas was added, the critical temperatures of the vessel skin and windows were approaching too close their design limit. It was decided to drop the pressure once again, and the experimental prognosis was reevaluated.

The initial startup transients of the system were readily observed mid-day on June 9th when the furnace was commanded to 500 °C. While the furnace reached steady state, the optics were aligned to give an average 1.2 V on both the reference and experimental detectors. This region was not without beam steering, as the steady state standard deviation of the reference signal was ±0.054 V and ±0.024 V for the experimental signal. This necessitated coherently averaging spectra for longer to reduce signal intensity issues. Expectedly, the measured process

pressure hardly changed with the furnace temperature as the system was vacuumed down, while the process thermocouples revealed the periodicity of the furnace control. As with the prior 6 kW furnace design, a single thermocouple is noted to diverge quickly from the bulk average. Namely, the TC1 reading exhibited a stronger dependency on the furnace oscillations, as well as reading roughly 200 °C higher than the average of the other thermocouples while the furnace was in stead state.

The skin temperatures were also seen to rise, however the insulating properties of the furnace were demonstrated as the skin temperature levelled to slightly over 100 °C on the interior. This same trend was observed for the window temperatures, however there was a clear bias in temperature distribution toward the access port side. The temperature bias was believed to be derivative of convective currents being initialized by the inflowing gas. The high thermal conductivity of the sapphire and the exterior window fitting cooling loops mitigate the windows from getting beyond their design limit. This kept the window temperatures at an average of 28 °C while the furnace was at steady state. The thermocouple reader is the same instrument used in the prior 6 kW furnace thermal characterization tests, and so the periodic dips in temperature are known to be solely electrical in nature.

Large variations in detector voltage were noticed when at elevated temperatures, which grew more severe when increasing the pressure. This was observed to be from a phenomena known as beam-steering where variations in gas indices of refraction (i.e. gas densities) divert the beam. When observing the outer sapphire windows with webcams, it was noted that the beam was moving in an estimated standard deviation of 2.54 cm on the window plane. To assist with data visualization, a moving average of 100 samples was applied to the data as indicated by the light traces in Figure 33 (e) on top of the raw data in the darker colors.

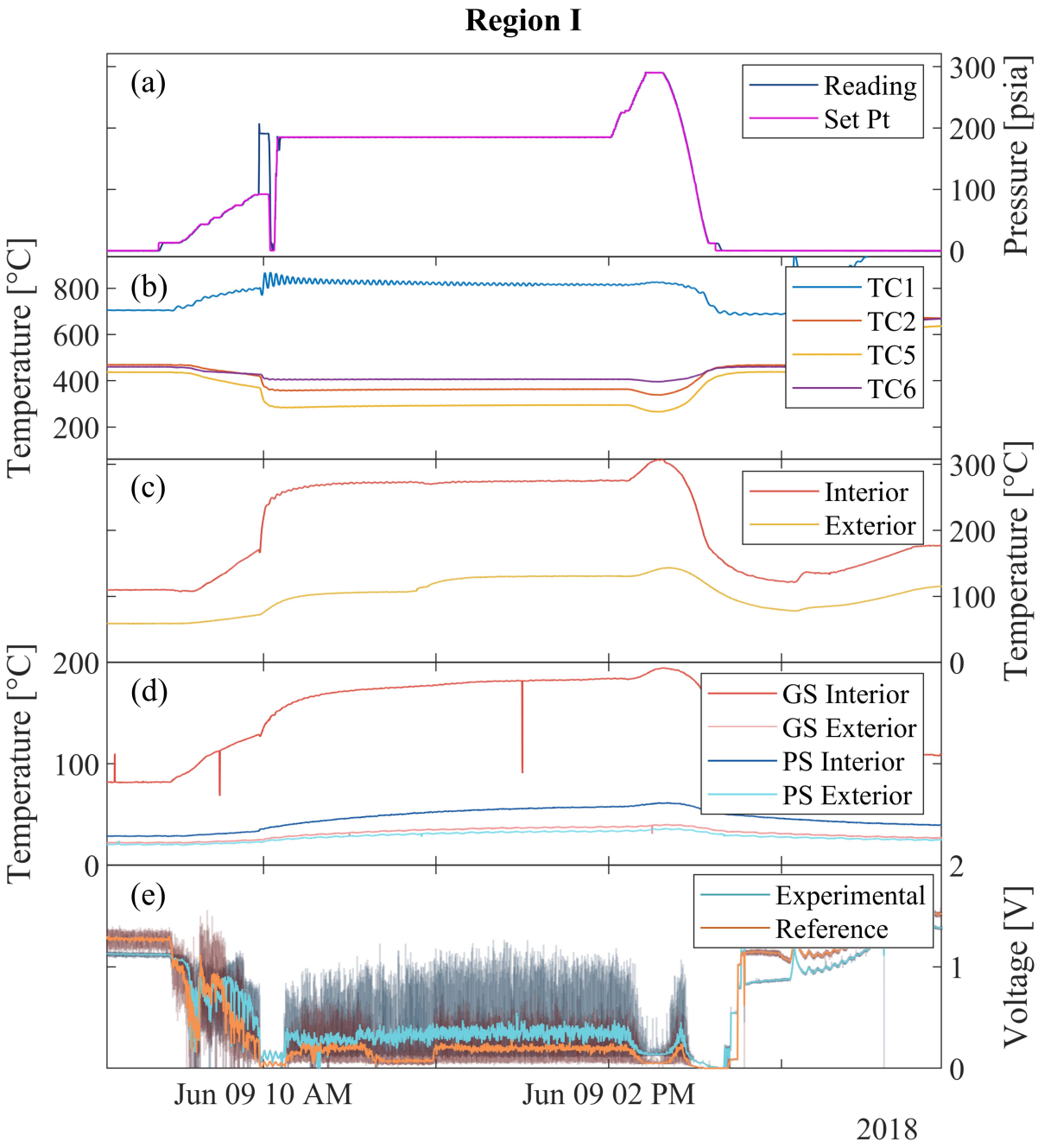

Fig. 33. Region I system metric readings. An error in setting the pressure on the experimental pressure controller resulted in a pressure spike at approximately 10 am in panel (a). The ringing of the furnace PID control, and subsequent drop of temperature in panel (b). The detector voltages are noted to drop severly with the application of pressure in (e).

At approximately 10 am during the first collection region, an error in setting the pressure controller resulted in a spike in pressure as gas was rapidly added to the system. The manifold was sealed off, the controller was readjusted to the proper setting, pressure was added to the manifold to be in equilibrium with the new system pressure, and operation was resumed. The dramatic effect of suddenly introducing a large amount of cold gas to the system is shown in Figure 33 (b) and Figure 33 (e). Without a bath gas pressure transducer, the exact amount of added gas was unknown. Damped oscillations of the furnace were observed with TC1, while the other thermocouple readings dropped nearly 50 °C. It should be noted that the thermocouple readings did not have heat transfer corrections applied, and they were simply raw readings. The interior skin and window temperatures were noted to have increased as well. There was a large, exponential decay, increase in the interior gas-side window temperature with a lesser increase in the power-side window interior measurement. This is likely indicative of the convective current initialization when injecting gas into the system, as mentioned previously.

Notably the temperature uniformity experienced a disparity as the pressure was increased. This trend was observed over multiple pressure increases, regardless of the rate of addition of the gas, and is directly opposed to the desired operation. As the pressure increased so did the rate of heat transfer, and with the bath gas being introduced from one side there was a longitudinal temperature gradient. However, the exact extent of the gradient was not able to be precisely determined due to differential thermal loading of the thermocouples. Disregarding TC1, the temperature was maintained to within 100 °C.

4.4.2. Spectral Data

A multitude of valuable absorption spectra were collected at various pressures and temperatures. Shown in Figure 34 is the experimental CO_2 absorption spectra from roughly 1595 nm to 1630 nm at increasing pressures and 296 K. Note that the shown spectra are baseline-corrected.

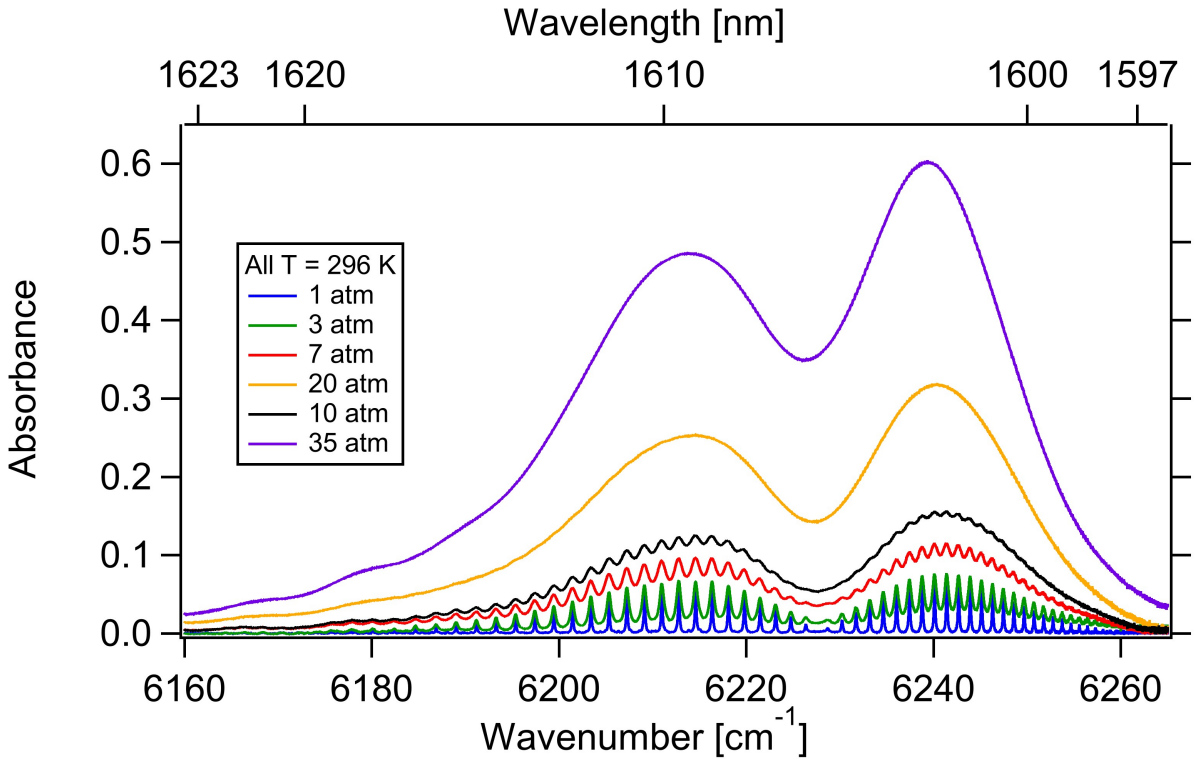

Fig. 34. Experimental CO_2 absorption spectra collected with the HTHP Cell at various pressures. This data was collected over June-July 2017, and demonstrates the effects of pressure broadening on absorption features.

The effect of pressure broadening is clearly evident as the absorption features of the P and R branches begin to blend together and form a smooth two-hump conjoined feature. This preliminary data demonstrates experimentally how pressure broadening can severly obscure the non-absorbing baseline. As the features blend and increase in absorbance, the parameters of the baseline become indeterminate as there is no zero-reference. This is in addition to the low

frequency oscillations in the comb intensity profile that occur over the span of hours that are common when trying to obtain extremely high SNR for spectral parameter estimation. Of course, a potential solution to this problem could be to collect a vacuum spectra before each experimental collection run, thereby determining both the nonuniform intensity profile as well as the affects of the physical optics. This quickly becomes prohibitive in the case of high pressure spectra, as the entire volume would need to be removed, and then a greater amount of gas volume added to move to the next higher pressure. This is also in addition to needing to reheat the added gas. The influence of temperature in combination of pressure on the absorption features was also observed, and is shown in the spectra comparison in Figure 35.

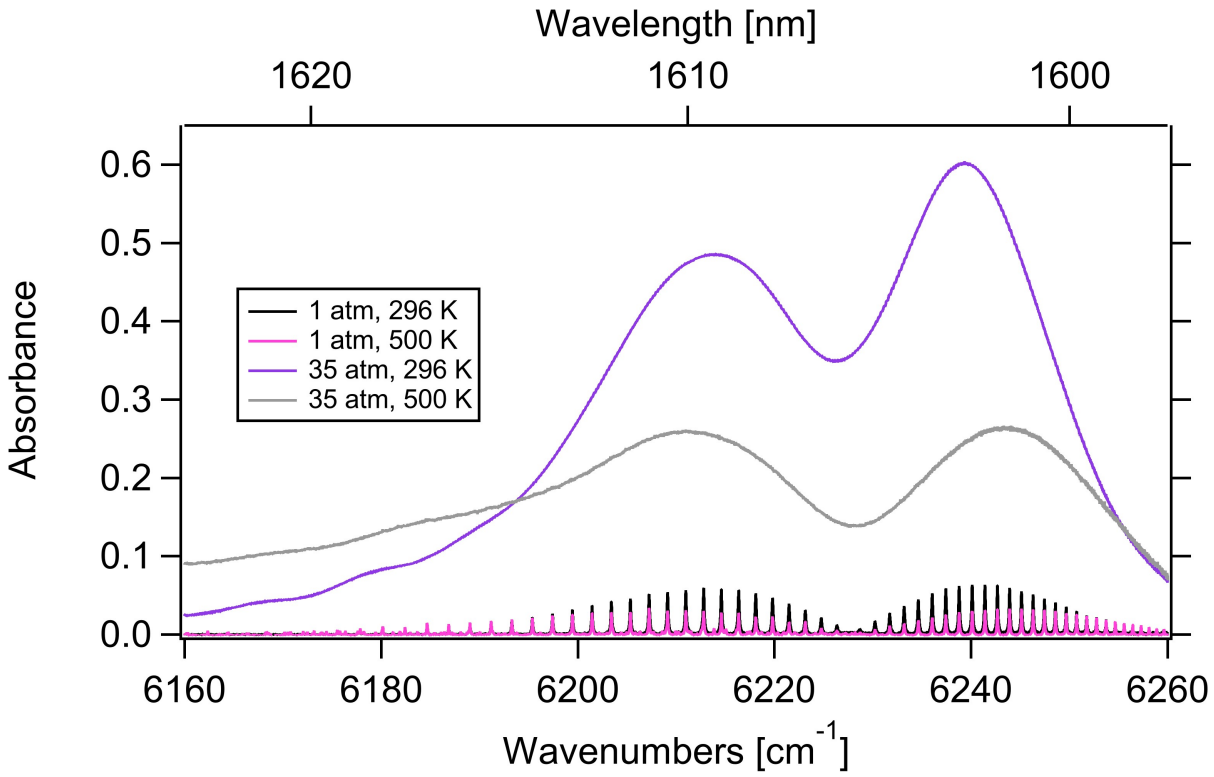

Fig. 35. Experimental CO_2 absorption spectra collected with HTHP Cell demonstrating influence of temperature and pressure. As the pressure increases, the absorption features are broadened and begin to blend. As temperature increases at room temperature, the absorbance decreases. This same result is observed when increasing temperature at elevated pressure, however the absorption feature tails are noted to exhibit a higher absorbance.

While the absorbance generally increases for higher pressure, the influence of temperature is noted to decrease and distribute the absorbance for this section of the CO_2 spectrum. It is believed that the increasing temperature distributes the energy across more quantum energy levels, opening more possible transitions.

4.5. System Conclusions

Overall, while the HTHP Cell experienced various thermal issues, it was still able to achieve unprecedented high temperature and high pressure performance for unique experimental spectra to be collected. Beginning with a rough conceptual idea, subcomponent design evolutions were discussed, along with failure analysis if applicable. Initial safety calculations were performed to determine human interaction limits and implement operating procedures. System characterization testing revealed the system is capable of achieving 41 atm at approximately 474 K. The charactization testing was facilitated through automated time series data collection. Operator useability to monitor and control the HTHP Cell was improved through the use of web-accessible data visualization tools. Increasing the pressure dramatically reduced thermal uniformity and performance. The configuration of how gas was injected into the system likely initialized convective currents within the pressure vessel interior volumes, which exacerbated heat transfer concerns.

5. CONCLUSIONS AND FUTURE WORK

5.1. Completed Work

In this thesis, we have demonstrated sub-millisecond DCS within a dynamic high pressure environment, and have developed an optical testbed for high temperature and pressure absorption model development. Existing spectral models and databases, which are instrumental in recovering thermodynamic properties from absorption measurements in unknown environments, are inaccurate at elevated temperature and pressures. The RCM measurements were largely unaffected by these uncertainties due to the modest temperature and pressure conditions in the system. Therefore, we were able to recover temperature of a CH_4-N_2 mixture at 704 μs time resolution. Absorption features were measured with 24345 comb teeth between 5167-6133 cm^{-1} due to the broadband nature of the dual-comb spectrometer. The measured temperature at the compression peak is 560 K, while an adiabatic simulation predicts 566 K. At later times, the difference between the measurement and simulation grows to 20 K, which may indicate the breakdown of the adiabatic assumption after the end of compression and the growth of cold boundary layers. In order to make measurements in more extreme environments, the existing absorption models and databases must be improved.

The optical testbed allows this expansion by creating a well known environment of high temperature and high pressure sample mixtures. This system features a pathlength of 45 cm and a design capability up to 100 atm and 1000 K. The subcomponent design evolution is presented, along with initial characterization tests of the performance. It was found that increased heat transfer at high pressure limits the range of operation of the current design. The primary cause of

the unwanted heat transfer is the coupling of pressure, convection, and conduction, and will be solved through future design modifications. This conclusion, and the results from characterization testing, was facilitated by automated time-series data collection and data visualization. Despite the system setbacks, absorption spectra of CO_2 was taken up to 35 atm at 500 K, and 7 atm at 750 K. DCS afforded large spectral bandwidths of spectra to be collected which allowed for the full dynamics of absorption feature broadening to be observed. Additionally, the inclusion of a reference beam allowed the non-absorbing baseline to be fully resolved. An improved accuracy such as this is essential for model and database development. This demonstrates the ability of the HTHP Cell to expand the current avenues of spectral models and databases.

5.2. Future Work

As mentioned above, future development of the HTHP cell will focus on implementations of new design alterations to allow the system to expand into its full design space. The primary focus of the design modifications are aimed at improving the heat transfer characteristics of the system, as well as increasing the temperature uniformity within the experimental spectroscopic cell. By addressing these primary concerns, it is believed that several of the other minor issues discussed in the body of this thesis will be further improved. Once these issues are resolved, numerous datasets will be collected at high pressures and temperatures, as well as with different gas mixture combinations. These datasets will be compared to existing spectral databases and models to give insight into the effectiveness of existing models at high pressures and temperatures as well as the improvements required to accurately model absorption

spectra in extreme conditions. These model improvements, and database expansions, created with the HTHP Cell will have far-reaching implications for the absorption spectroscopy community. Additionally, with the advent of mode-locked mid-IR frequency combs, the HTHP Cell also will also allow for another regime of molecules and dynamics to be explored. With enhanced absorption models in the near and mid infrared, more harsh environments can be measured with laser absorption spectroscopy, allowing the techniques developed for the RCM temperature measurement to be additionally implemented.

The RCM techniques presented will also have enhanced applicability when combined with mid-IR mode-locked dual-comb technology. Leveraging the stronger absorption cross section characteristics of active molecules in the mid-IR affords additionaly combustion-relavent species to be measured. This also has implications of increased sensitivity. The increase in sensitivity will then empower multi-species thermodynamic property measurements at higher time resolution with a single spectrometer. Together these systems enable progress toward fast DCS in dynamic high pressure systems.

BIBLIOGRAPHY

1. P. J. Schroeder, R. J. Wright, S. Coburn, B. Sodergren, K. C. Cossel, S. Droste, G. W. Truong, E. Baumann, F. R. Giorgetta, I. Coddington, N. R. Newbury, and G. B. Rieker, "Dual frequency comb laser absorption spectroscopy in a 16 MW gas turbine exhaust," Proc. Combust. Inst. **36**(3), 4565–4573 (2017).
2. P. J. Schroeder, D. J. Pfotenhauer, J. Yang, F. R. Giorgetta, W. C. Swann, I. Coddington, N. R. Newbury, and G. B. Rieker, "High temperature comparison of the HITRAN2012 and HITEMP2010 water vapor absorption databases to frequency comb measurements," J. Quant. Spectrosc. Radiat. Transf. **203**, 194–205 (2017).
3. J. Peralta, Y. J. Lee, K. McGouldrick, H. Sagawa, A. Sánchez-Lavega, T. Imamura, T. Widemann, and M. Nakamura, "Overview of useful spectral regions for Venus: An update to encourage observations complementary to the Akatsuki mission," Icarus **288**, 235–239 (2017).
4. J. Tennyson and S. N. Yurchenko, "Laboratory spectra of hot molecules: Data needs for hot super-Earth exoplanets," Mol. Astrophys. **8**, 1–18 (2017).
5. C. S. Goldenstein, R. M. Spearrin, J. B. Jeffries, and R. K. Hanson, "Infrared laser-absorption sensing for combustion gases," Prog. Energy Combust. Sci. **60**, 132–176 (2017).
6. R. K. Hanson, R. M. Spearrin, and C. S. Goldenstein, *Spectroscopy and Optical Diagnostics for Gases* (Springer International Publishing, 2016).
7. P. R. Griffiths and J. A. D. Haseth, *Fourier Transform Infrared Spectrometry* (John Wiley & Sons, 2007).

8. H. Tran, D. Bermejo, J.-L. Domenech, P. Joubert, R. R. Gamache, and J.-M. Hartmann, "Collisional parameters of H2O lines: Velocity effects on the line-shape," J. Quant. Spectrosc. Radiat. Transf. **108**(1), 126–145 (2007).

9. G. B. Rieker, X. Liu, H. Li, J. B. Jeffries, and R. K. Hanson, "Measurements of near-IR water vapor absorption at high pressure and temperature," Appl. Phys. B **87**(1), 169–178 (2007).

10. G. B. Rieker, J. B. Jeffries, and R. K. Hanson, "Measurements of high-pressure CO2 absorption near 2.0 μm and implications on tunable diode laser sensor design," Appl. Phys. B **94**(1), 51–63 (2009).

11. I. Coddington, N. Newbury, and W. Swann, "Dual-comb spectroscopy," Optica **3**(4), 414 (2016).

12. J. L. Hall, "Nobel Lecture: Defining and measuring optical frequencies," Rev. Mod. Phys. **78**(4), 1279–1295 (2006).

13. T. Kobayashi, T. Sueta, Y. Cho, and Y. Matsuo, "High-repetition-rate optical pulse generator using a Fabry-Perot electro-optic modulator," Appl. Phys. Lett. **21**(8), 341–343 (1972).

14. D. A. Long, A. J. Fleisher, K. O. Douglass, S. E. Maxwell, K. Bielska, J. T. Hodges, and D. F. Plusquellic, "Multiheterodyne spectroscopy with optical frequency combs generated from a continuous-wave laser," Opt. Lett. **39**(9), 2688–2690 (2014).

15. D. R. Carlson, D. D. Hickstein, W. Zhang, A. J. Metcalf, F. Quinlan, S. A. Diddams, and S. B. Papp, "An ultrafast electro-optic light source with sub-cycle precision," ArXiv171108429 Phys. (2017).

16. I. Coddington, W. C. Swann, and N. R. Newbury, "Coherent dual-comb spectroscopy at high signal-to-noise ratio," Phys. Rev. A **82**(4), 043817 (2010).
17. G. B. Rieker, F. R. Giorgetta, W. C. Swann, J. Kofler, A. M. Zolot, L. C. Sinclair, E. Baumann, C. Cromer, G. Petron, C. Sweeney, P. P. Tans, I. Coddington, and N. R. Newbury, "Frequency-comb-based remote sensing of greenhouse gases over kilometer air paths," Optica **1**(5), 290–298 (2014).
18. N. R. Newbury, I. Coddington, and W. Swann, "Sensitivity of coherent dual-comb spectroscopy," Opt. Express **18**(8), 7929–7945 (2010).
19. S. S. Goldsborough, S. Hochgreb, G. Vanhove, M. S. Wooldridge, H. J. Curran, and C.-J. Sung, "Advances in rapid compression machine studies of low- and intermediate-temperature autoignition phenomena," Prog. Energy Combust. Sci. **63**(Supplement C), 1–78 (2017).
20. G. Mittal and C.-J. Sung, "Aerodynamics inside a rapid compression machine," Combust. Flame **145**(1), 160–180 (2006).
21. B. W. Weber, C.-J. Sung, and M. W. Renfro, "On the uncertainty of temperature estimation in a rapid compression machine," Combust. Flame **162**(6), 2518–2528 (2015).
22. E. F. Nasir and A. Farooq, "Time-resolved temperature measurements in a rapid compression machine using quantum cascade laser absorption in the intrapulse mode," Proc. Combust. Inst. **36**(3), 4453–4460 (2017).
23. C. L. Hagen and S. T. Sanders, "Investigation of multi-species (H 2 O 2 and H 2 O) sensing and thermometry in an HCCI engine by wavelength-agile absorption spectroscopy," Meas. Sci. Technol. **18**(7), 1992 (2007).

24. L. A. Kranendonk, J. W. Walewski, T. Kim, and S. T. Sanders, "Wavelength-agile sensor applied for HCCI engine measurements," Proc. Combust. Inst. **30**(1), 1619–1627 (2005).

25. T. Werblinski, P. Fendt, L. Zigan, and S. Will, "High-speed combustion diagnostics in a rapid compression machine by broadband supercontinuum absorption spectroscopy," Appl. Opt. **56**(15), 4443–4453 (2017).

26. T. Werblinski, S. Kleindienst, R. Engelbrecht, L. Zigan, and S. Will, "Supercontinuum based absorption spectrometer for cycle-resolved multiparameter measurements in a rapid compression machine," Appl. Opt. **55**(17), 4564–4574 (2016).

27. "Measurements and modelling of high pressure pure CO 2 spectra from 750 to 8500cm -1. I-central and wing regions of the allowed vibrational bands | Request PDF," https://www.researchgate.net/publication/230602807_Measurements_and_modelling_of_high_pressure_pure_CO_2_spectra_from_750_to_8500cm_-1_I-central_and_wing_regions_of_the_allowed_vibrational_bands.

28. S. Stefani, G. Piccioni, M. Snels, D. Grassi, and A. Adriani, "Experimental CO2 absorption coefficients at high pressure and high temperature," J. Quant. Spectrosc. Radiat. Transf. **117**, 21–28 (2013).

29. C. Brodbeck, N. Van-Thanh, J.-P. Bouanich, C. Boulet, A. Jean-Louis, B. Bezard, and C. de Bergh, "Measurements of pure CO2 absorption at high densities near 2.3 μm," J. Geophys. Res. Planets **96**(E2), 17497–17500 (1991).

30. C. Christiansen, T. Stolberg-Rohr, A. Fateev, and S. Clausen, "High temperature and high pressure gas cell for quantitative spectroscopic measurements," J. Quant. Spectrosc. Radiat. Transf. **169**, 96–103 (2016).

31. M. Y. Perrin and J. M. Hartmann, "Temperature-dependent measurements and modeling of absorption by CO2-N2 mixtures in the far line-wings of the 4.3μm CO2 band," J. Quant. Spectrosc. Radiat. Transf. **42**(4), 311–317 (1989).

32. J. Hartmann and C. Boulet, "Line mixing and finite duration of collision effects in pure CO2 infrared spectra: Fitting and scaling analysis," J. Chem. Phys. **94**(10), 6406–6419 (1991).

33. J. M. Hartmann, M. Y. Perrin, Q. Ma, and R. H. Tippings, "The infrared continuum of pure water vapor: Calculations and high-temperature measurements," J. Quant. Spectrosc. Radiat. Transf. **49**(6), 675–691 (1993).

34. A. Predoi-Cross, A. D. May, A. Vitcu, J. R. Drummond, J.-M. Hartmann, and C. Boulet, "Broadening and line mixing in the 2000←0110, 1110←0000 and 1220←0110 Q branches of carbon dioxide: Experimental results and energy-corrected sudden modeling," J. Chem. Phys. **120**(22), 10520–10529 (2004).

35. A. Farooq, J. B. Jeffries, and R. K. Hanson, "Measurements of CO_2 concentration and temperature at high pressures using 1*f*-normalized wavelength modulation spectroscopy with second harmonic detection near 2.7 μm," Appl. Opt. **48**(35), 6740–6753 (2009).

36. V. Nagali and R. K. Hanson, "Design of a diode-laser sensor to monitor water vapor in high-pressure combustion gases," Appl. Opt. **36**(36), 9518–9527 (1997).

37. B. Winters, *LINE SHAPE IN THE WING BEYOND THE BAND HEAD OF THE 4.3 MICRON BAND OF CO2,* (CATHOLIC UNIV OF AMERICA WASHINGTON DC, 1963).

38. D. E. Burch, D. A. Gryvnak, R. R. Patty, and C. E. Bartky, "Absorption of Infrared Radiant Energy by CO_2 and H_2O. IV. Shapes of Collision-Broadened CO_2 Lines*," JOSA **59**(3), 267–280 (1969).

39. T. M. Petrova, A. M. Solodov, A. A. Solodov, and V. I. Starikov, "Line mixing in some water vapor transitions perturbed by N2, Ar and He pressure," J. Mol. Struct. **1080**, 63–68 (2015).

40. S. Coburn, C. B. Alden, R. Wright, K. Cossel, E. Baumann, G.-W. Truong, F. Giorgetta, C. Sweeney, N. R. Newbury, K. Prasad, I. Coddington, and G. B. Rieker, "Regional trace-gas source attribution using a field-deployed dual frequency comb spectrometer," Optica **5**(4), 320–327 (2018).

41. A. Boissiere, "Effect of additives on laser ignition and compression ignition of methane and hydrocarbons in a rapid compression machine," ProQuest Dissertations Publishing (2016).

42. C. Dumitrache, M. Baumgardner, A. Boissiere, A. Maria, J. Roucis, A. J. Marchese, and A. Yalin, "A study of laser induced ignition of methane–air mixtures inside a Rapid Compression Machine," Proc. Combust. Inst. **36**(3), 3431–3439 (2017).

43. G.-W. Truong, E. M. Waxman, K. C. Cossel, E. Baumann, A. Klose, F. R. Giorgetta, W. C. Swann, N. R. Newbury, and I. Coddington, "Accurate frequency referencing for fieldable dual-comb spectroscopy," Opt. Express **24**(26), 30495–30504 (2016).

44. I. E. Gordon, L. S. Rothman, C. Hill, R. V. Kochanov, Y. Tan, P. F. Bernath, M. Birk, V. Boudon, A. Campargue, K. V. Chance, B. J. Drouin, J.-M. Flaud, R. R. Gamache, J. T. Hodges, D. Jacquemart, V. I. Perevalov, A. Perrin, K. P. Shine, M.-A. H. Smith, J. Tennyson, G. C. Toon, H. Tran, V. G. Tyuterev, A. Barbe, A. G. Császár, V. M. Devi, T. Furtenbacher, J. J. Harrison, J.-M. Hartmann, A. Jolly, T. J. Johnson, T. Karman, I. Kleiner,

A. A. Kyuberis, J. Loos, O. M. Lyulin, S. T. Massie, S. N. Mikhailenko, N. Moazzen-Ahmadi, H. S. P. Müller, O. V. Naumenko, A. V. Nikitin, O. L. Polyansky, M. Rey, M. Rotger, S. W. Sharpe, K. Sung, E. Starikova, S. A. Tashkun, J. V. Auwera, G. Wagner, J. Wilzewski, P. Wcisło, S. Yu, and E. J. Zak, "The HITRAN2016 molecular spectroscopic database," J. Quant. Spectrosc. Radiat. Transf. **203**, 3–69 (2017).

45. R. V. Kochanov, I. E. Gordon, L. S. Rothman, P. Wcisło, C. Hill, and J. S. Wilzewski, "HITRAN Application Programming Interface (HAPI): A comprehensive approach to working with spectroscopic data," J. Quant. Spectrosc. Radiat. Transf. **177**, 15–30 (2016).
46. C. Morley, *GASEQ* (2005).
47. A. P. Mouritz, ed., "1 - Introduction to aerospace materials," in *Introduction to Aerospace Materials* (Woodhead Publishing, 2012), pp. 1–14.
48. "Power Generation | Special Metals Company," http://www.specialmetals.com/markets/power-generation.html.
49. A. P. Mouritz, ed., "20 - Fatigue of aerospace materials," in *Introduction to Aerospace Materials* (Woodhead Publishing, 2012), pp. 469–497.
50. "Inconel Alloy 740H | PCC Energy Group," http://www.pccenergy.com/markets/power-generation/inconel-alloy-740h.html.
51. "TESCOM™ 44-4000 Series Spring Diving Regulator | Emerson US," https://www.emerson.com/en-us/catalog/tescom-44-4000.
52. I. Coddington, W. C. Swann, and N. R. Newbury, "Coherent Multiheterodyne Spectroscopy Using Stabilized Optical Frequency Combs," Phys. Rev. Lett. **100**(1), 013902 (2008).

53. M. A. Kelley, M. S. Jakulewicz, C. B. Dreyer, T. E. Parker, and J. M. Porter, "System overview and characterization of a high-temperature, high-pressure, entrained-flow, laboratory-scale gasifier," Rev. Sci. Instrum. **86**(5), 055106 (2015).
54. "InfluxDB | The Time Series Database in the TICK Stack," https://www.influxdata.com/time-series-platform/influxdb/.
55. S. N. Zehra, "Time Series Databases and InfluxDB," 45 (n.d.).
56. "Grafana - The open platform for analytics and monitoring," https://grafana.com/.
57. "Sapphire Windows," https://www.thorlabs.com/NewGroupPage9.cfm?ObjectGroup_ID=3982.
58. "Appendix B: Equations for Determining the Energy of Explosion," in *Understanding Explosions* (John Wiley & Sons, Inc., 2010), pp. 169–172.
59. M. M. Swisdak, "Simplified Kingery Airblast Calculations," 18 (n.d.).
60. J. R. Franks, M. R. Stephenson, and C. J. Merry, "PREVENTING OCCUPATIONAL HEARING LOSS — A PRACTICAL GUIDE —," 106 (n.d.).
61. "THE EFFECTS OF NUCLEAR WEAPONS," 660 (n.d.).
62. R. B. Bird, *Transport Phenomena* (New York : Wiley, 1960).
63. "Engineering Simulation & 3D Design Software | ANSYS," https://www.ansys.com/.

APPENDIX

A. Temperature Uniformity Characterization and Furnace Change

As part of the furnace design evolution, various subcomponent performance tests were performed to iteratively verify subcomponent functionality. These tests then directly resulted in design changes or modifications that impacted the final design. A temperature profile test was performed on August 24, 2017 where the system was commanded to maintain a high temperature and the temperature distribution evaluated. The pressure vessel had N_2 gas flowed through the system for a few hours in order to assure a relatively pure N_2 bath gas. The quartz optical cell was filled with N_2 as well, and the furnace was commanded to 200 °C at a rate of 100 °C/hr. Likely due to the large empty internal volumes, as well as relatively cold gas injection, convective currents developed within either side of the pressure vessel, causing an exorbitant amount of heat to be lost. This amount of heat was determined to be greater than the 6 kW furnace could supply because at 100% duty cycle the temperature was slowly decreasing. In general, operating electric furnaces at 100% duty cycle reduces the overall system life and so the furnace power was commanded lower shortly after observing the heat loss phenomenon. Hotspot formation was also noticed through thermal imaging, which is shown in Figure 36.

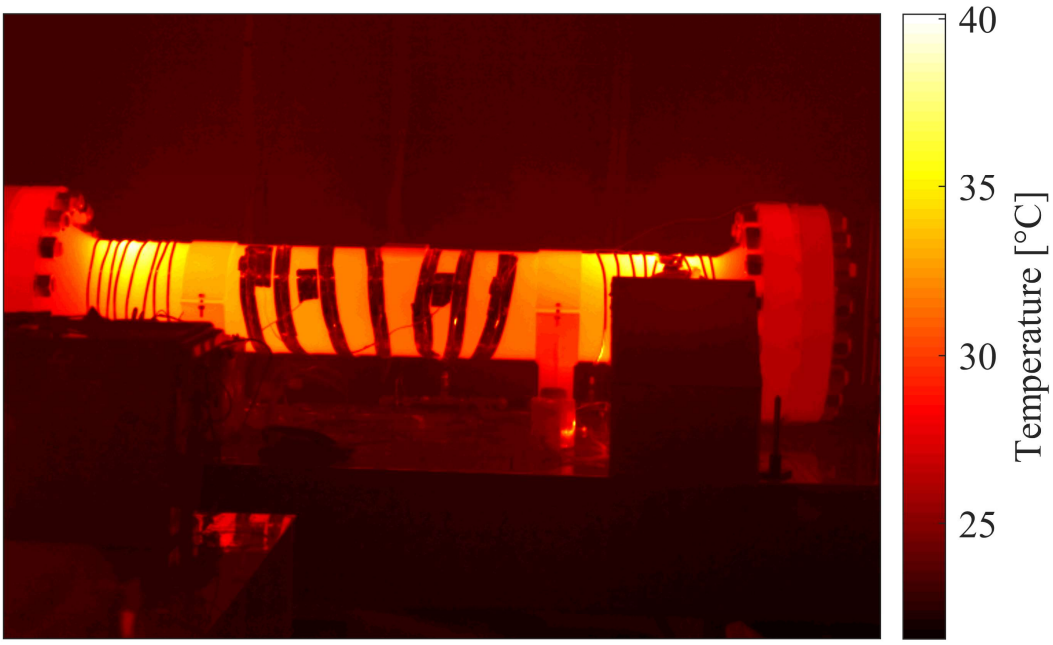

Fig. 36. Thermogram of pressure vessel during temperature characterization test on Aug 24th, 2017. Exterior cooling loops are shown in thick lines on either side of the vessel, and heat tape is attached to the center of the vessel with aluminum tape. Hotspots are noted on either side of the vessel corresponding to relatively large empty volumes. The pressure vessel saddles are also noted to be roughly 10 °C above the ambient temperature.

It is also noted that the hotspot formation trends hotter toward the top middle of the pressure vessel on either end, as expected for convection around a cylinder. This hypothesis was verified using a first order analysis. The Rayleigh number determines if heat transfer is primarily through convection when greater than a critical value given a diameter-length ratio for horizontal circular cavities. The Rayleigh number, Ra, is given below in Eq. (5.8) where g is gravity, β is the volume expansion coefficient, $T_h - T_c$ is the temperature difference, L is the characteristic length, ν is the kinematic viscosity, and α is the thermal diffusivity coefficient.

$$Ra = \frac{g\beta(T_h - T_c)L^3}{\nu\alpha} \qquad (5.1)$$

For the D/L of 0.677 for each empty cavity of the pressure vessel, the critical Rayleigh value is given as $Ra_{crit} = 22{,}364$. To determine an upper value for convection at the worst case of 100 atm, N_2 bath gas values from Refprop were calculated for a temperature difference of 112 K. This temperature difference was determined by internal and external thermocouple readings. The Rayleigh value was calculated to be much higher than the critical value, indicating a strong convective heat transfer dependence. A relatively high degree of heat transfer through the vessel saddles was also observed. The local area around the saddle mount points to the optical table were warm to the touch, and the thermal image shows a roughly 10 °C temperature difference. The thermal resistances for the saddles are also roughly three times less than for exterior convective heat transfer, indicating that thermal breaks should be added. It is likely that the optical table was acting as a large heatsink as the top is thermally conductive steel. During the August 24th test, anomalies were also noticed on thermocouple readings and a few of the internal temperature measurements are shown in Figure 37.

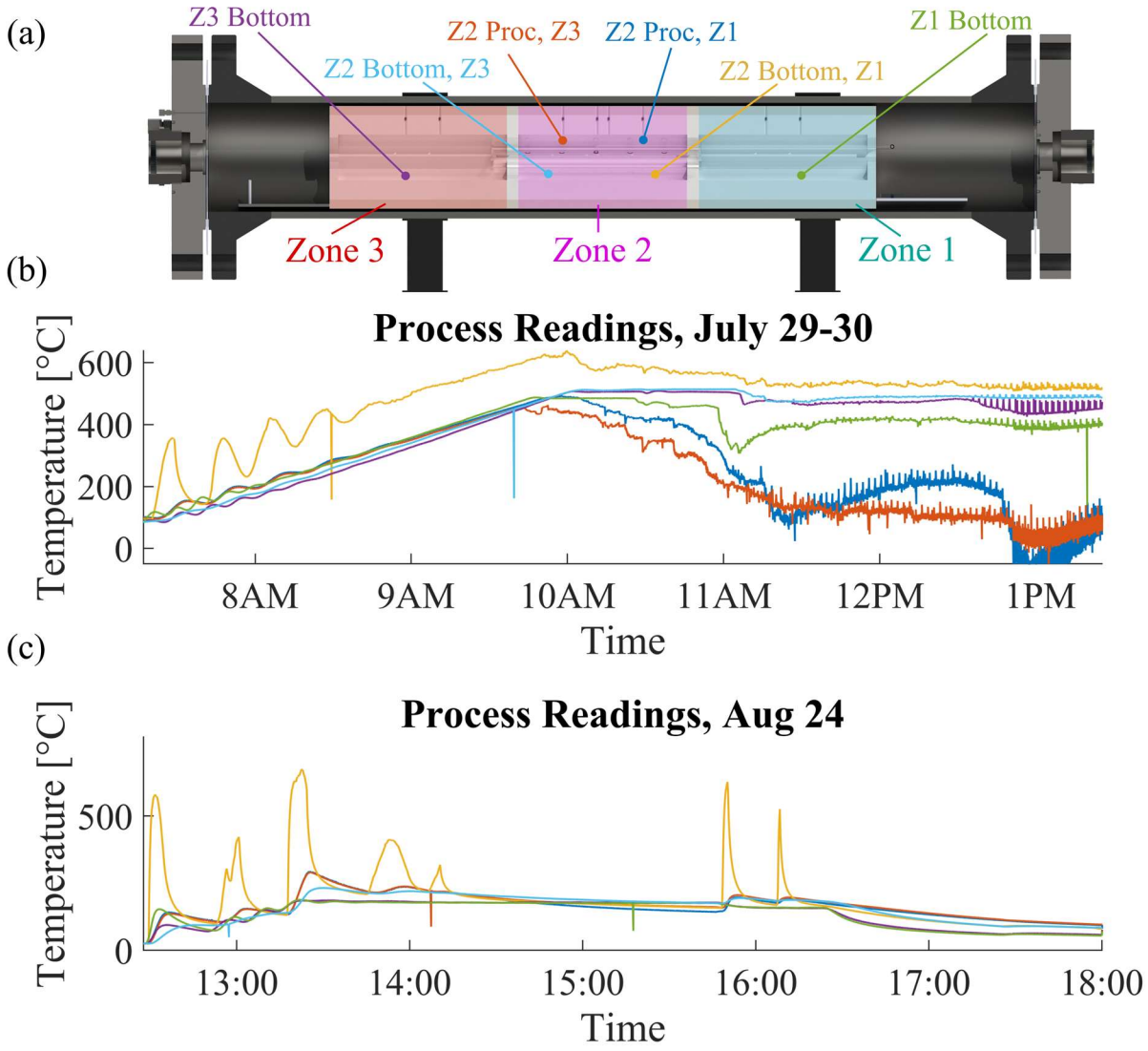

Fig. 37. Thermocouple locations and temperature data for data collection and temperature characterization test. (a) Thermocouple locations, along with furnace zones. (b) Thermocouple data for data collection on July 30th, 2017. TC1 is noted to consistently read higher temperature, while electrical issues begin at approximately 10am. (c) Temperature characterization test showing relative suppression of electrical issues, however TC1 readings were again higher and strongly correlated with furnace duty cycle. The progression from (b) to (c) demonstrated that the TC1 reading tip was getting hotter.

During the July 29-30th collection, at approximately 10 am, electrical issues began to corrupt the sensor readings causing them to diverge significantly from reality. While this seemingly plagued all of the thermocouples, the Z2-process-Z1-side, and Z2-bottom-Z1-side,

thermocouples remained fairly self consistent. These electrical issues were known prior to the experiments, however the degree of severity was not observed until a multi-hour experiment was underway. Before the August 24th test it was discovered that restarting the Omega DP1001AM thermocouple readers appeared to clear the issue. The electrical issue is believed to be originating in grounding loops that interfere with the reader reference voltage, exacerbated by the AC nature of the furnace control. Further testing signified the sensitivity of the readers, as touching thermocouples, the optical table, or the pressure vessel would cause shifts of up to 10 °C in the readings. While the spurious sharp dips in readings are also due to intermittent electrical connectivity issues, the progressively increasing temperature spikes for the Z2-bottom-Z1-side thermocouple are indicative of a larger issue. It was also observed that the thermocouple exhibited greater sensitivity to the furnace duty cycle, but due to the prior electrical issues the progressively increasing sensitivity was attributed to faulty wiring. Unfortunately during the August 24th test the furnace fuse blew and forced the execution of system shutdown procedures. During post-mortem analysis of the furnace failure, it was concluced that the Z2-bottom-Z1-side thermocouple reached too close to a furnace element and caused a hotspot that melted through the Nichrome wire. A view of the suspect thermocouple and its location within the 6 kW furnace is shown in Figure 38.

(a) (b)

Fig. 38. Views of thermocouples within 6 kW furnace, and probable burn mark. (a) Power-side view of the thermocouple locations within 6 kW furnace, with the TC1 location indicated by the red circle. Image was taken after characterization test, and metal warping is noted. (b) Closer view of probable burn mark on TC1 indicated by red circle.

Upon closer inspection it was found that the metal-sheathed thermocouples had fatigued over time, and their own weight caused enough warping to deflect the end by roughly 2.5 cm. By design the sheaths were grounded, however this immediately caused a short circuit when the metal sheat contacted the resistance coil. As the resistance coils were connected in series, and were embedded within cured insulation, it would have first required removing the majority of the interior insulation. The burned-out region could have been brazed together, or potentially welded, however this would create a local region of increased resistance. Subsequently the desired temperature uniformity would be disrupted. Instead, it was concluded that new higher power, more robust, furnace would be installed.

B. *New Furnace Thermocouple Locations*

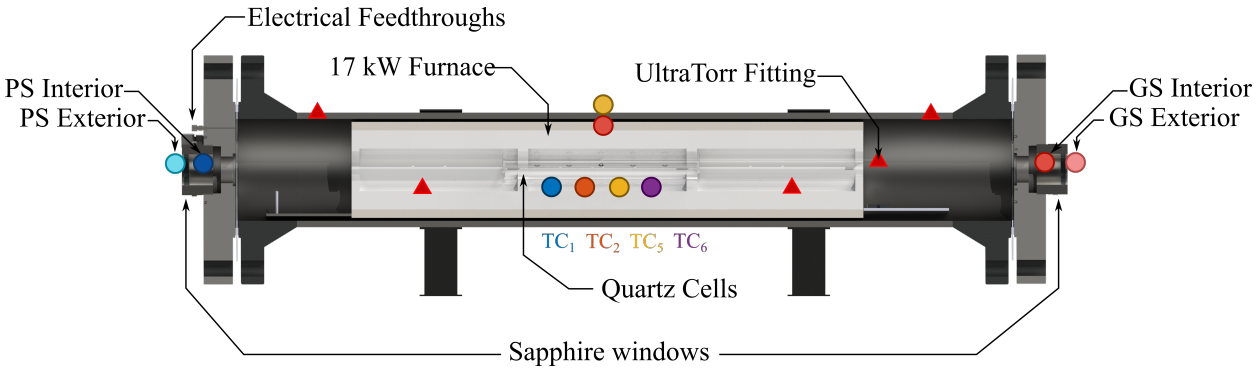

Fig. 39. Thermocouple locations within new furnace design. Process-Side (PS) thermocouples are located on the left of the HTHP Cell, while the Gas-Side (GS) thermocouples are on the right. The process thermocouples; TC1, TC2, TC5, and TC6, are located just below the spectroscopic cells in the center of the furnace assembly.

C. *June 2018 System Performance Tests*

During the June 2018 spectra collection, three distinct regions of operation are denoted and Regions II and III are discussed here. These are partitioned primarily based on pressure operation. Region II is shown in Figure 40.

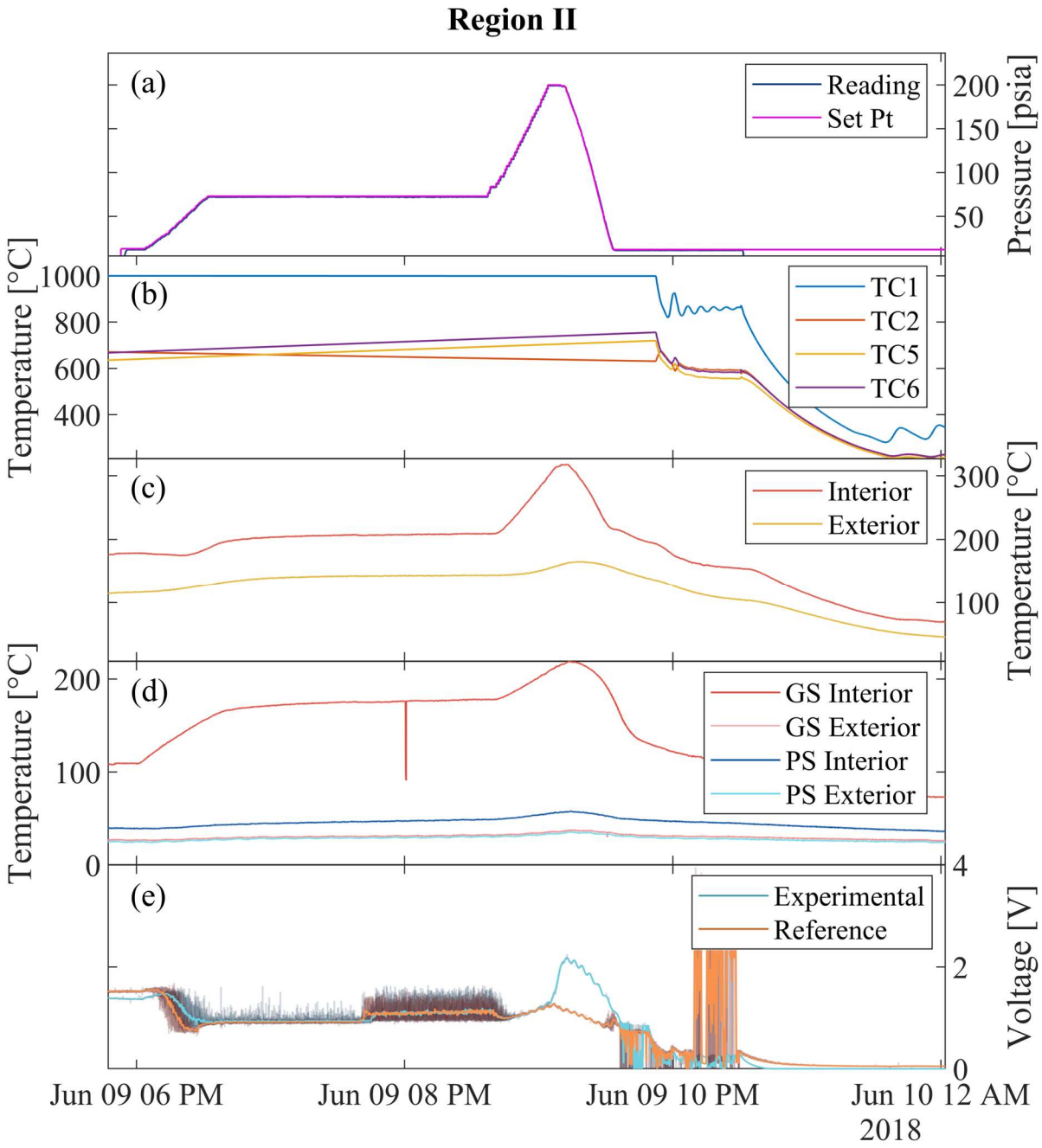

Fig. 40. Region II data collection range. Electrical issues caused process temperature readings to become corrupted for majority of collection in (b). However, the strong correlation between pressure and skin and window temperature is shown in (c) and (d). Detector voltages in (e) are noted to oscillate from pressure oscillations. The magnitude of oscillation is too small to be seen on the scale of panel (a). Lastly, the voltage varies wildly then drops to zero as the system unaligns from the prior high temperature and pressure set point.

While the process thermocouple readings were not available for the majority of Region II due to an anomaly with the data acquisition system, there was still valuable information that was gleaned from the other measurements. As seen in Region I, the system is relatively thermally stable while in steady state below 100 psi, and the detector voltages remained high at roughly 1.0 V. Slight adjustments were made to the alignment through the piezoelectric motors to adjust the voltage to roughly 1.2 V during operation.

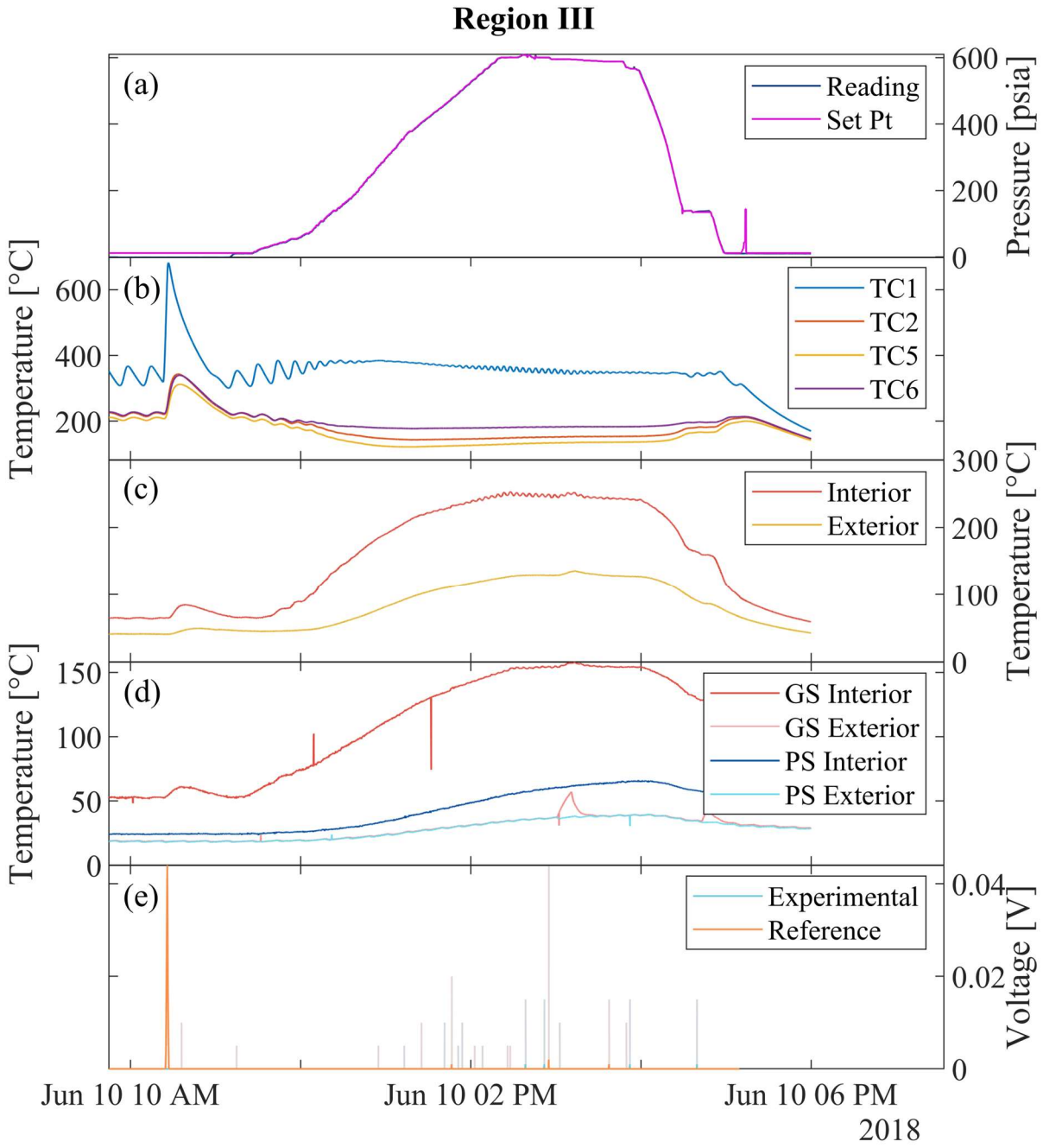

Fig. 41. Region III of June 2018 data collection. This test did not predicate upon data collection, and was meant to determine the highest achievable pressure for a given temperature. Resonance was observed in the experimental quartz cell, together with the process temperatures as indicated by panel (b), which halted the experiment. It was confirmed at roughly 5 pm that a rupture had occurred within one of the quartz cells allowing the bath gas to leak into the cell.

In Region III, shown in Figure 41, the pressure was increased while keeping the furnace at 200 °C in an attempt to probe the maximum possible pressure while at a slight elevation of temperature. The system was able to achieve roughly 41 atm of pressure before the interior skin temperature, and gas-side window temperature, were approaching the design limitations. The end-of-test procedures were conducted shortly after this to conclude the experiment.